Physics of tearing mode rotation slow-down in the RFX-mod tokamak

L. Cordaro[1], P. Zanca[1], M. Zuin[1,2], F. Auriemma[1,2], A. Fassina[1,2], E. Martines[1,3], B. Zaniol[1], R. Cavazzana[1], G. De Masi[1,2], G. Grenfell[1], B. Momo[1], S. Spagnolo[1], M. Spolaore[1,2] and N. Vianello[1,2]

[1]Consorzio RFX (CNR, ENEA, INFN, University of Padova, Acciaierie Venete SpA), corso Stati Uniti 4, Padova, Italy
[2]CNR-ISTP, Padova, Italy
[3] Department of Physics "Giuseppe Occhialini", University of Milan – Bicocca, Piazza della Scienza 3, 20126 Milan, Italy

E-mail: `luigi.cordaro@igi.cnr.it`

Abstract. We present a study of the fast, spontaneous rotation regime of tearing modes in the RFX-mod circular tokamak discharges. Integrated analyses of magnetic, flow and kinetic measurements, are discussed. This analysis of rotation frequency components related to the ion flow and diamagnetic drift shows that the tearing mode fast rotation is mainly driven by the diamagnetic drift. In particular, the global decrease of the temperature profile, induced by a growing mode amplitude, can explain the slowing-down of the rotation, which in turn can trigger a potentially disruptive sequence. We show that in RFX-mod the slowing-down cannot be explained solely on the basis of the electromagnetic torque with the external conductive structures, as often reported in literature from other experiments.
Statistical analysis of disruptions with slowing down islands shows that tearing modes take a part in the disruption, even without a locking to the wall.

1. Introduction

Tearing modes (TMs) are resistive magnetohydrodynamics instabilities [1] observed both in Tokamak and Reversed Field Pinch (RFP) fusion devices. A (m, n) TM, being m and n the poloidal and toroidal mode numbers respectively, is characterized by a helical magnetic island, generated through magnetic reconnection by current structures flowing at the resonant surface, located at the radius r_s where the condition $q(r_s) = m/n$ is fulfilled (q is the safety factor).

TMs are a concern for fusion plasmas, as the topology of the associated magnetic islands locally flatten the pressure profile and increase particle and energy radial transport. Therefore, large magnetic islands lead to confinement degradation. TMs are a major obstacle towards the achievement of high-performance fusion plasmas. Mode amplitude and the related detrimental effects are mitigated by the spontaneous rotation with the plasma. In fact, mirror currents induced onto the surrounding wall(s), always having finite conductivity, screen the radial field therein. However, the electromagnetic torque developed by the interaction between TM and these mirror currents can stop TM rotation in the laboratory frame (wall-locking) as soon as the amplitude exceeds a certain threshold [2, 3]. When this occurs, the stabilizing effect of the wall(s) is lost, and the TM amplitude increases at a rate given by the wall(s) resistive time constant(s). This phenomenon usually leads to a rapid termination of the discharge (disruption).

In tokamak, TMs are often seen to rotate with the electron fluid [4]. This phenomenon has been also observed in low plasma current ($I_p < 100kA$) RFP discharges of RFX-mod (RFX-mod plasma can have I_p up to $2MA$ in RFP configuration), where TM spontaneous rotation can occur due to the small amplitudes in such low current conditions [5]. In these cases, TM frequencies differ from the ion fluid rotation frequency, owing to the diamagnetic drift.

The present paper mainly discusses the connection between TM frequencies, as detected by large-bandwidth pick-up magnetic probes, located inside the vacuum-vessel, and flow velocity, as reconstructed from spectroscopic and kinetic measurements, in RFX-mod ohmic circular tokamak discharges (a=0.459m, R_0=2m, $B_\phi \leq 0.55T$, $I_p \leq 100kA$).

We will show that the diamagnetic drift provides the dominant contribution to TM frequency. Moreover, the spin-up/slow-down observed in conjunction with TM amplitude decrease/increase is hardly explained purely in terms of a torque balance model taking into account the electromagnetic interaction with the conductive wall. Instead, we will provide clear indications that this dynamics is related to mode-island-induced modifications of the kinetic profiles (mainly temperature), which determine the diamagnetic drift. To our knowledge this is not a standard interpretation of the TM rotational dynamics, hence the analyses here reported can be regarded as new results.

The paper is organized as described in the following.

In section 2, the adopted techniques for the detection and characterization of TMs, both in terms of amplitude and rotation frequency, based on the in-vessel magnetic measurements, are presented. The Fourier analysis of the pick-up probes signals will

be adequately interpreted in terms of a standard MHD model based on the cylindrical Newcomb's equation [2, 3]. This allows an extrapolation of the edge measurements to obtain an estimate of the island width inside the plasma. A new statistical analysis of disruptions marked by TMs will confirm previous results obtained with out-vessel low frequency probes [6]. In section 3 the ion-flow and diamagnetic components of the TM rotation frequency will be identified, and compared to the previous magnetic analyses on the basis of a two-fluid phenomenological model. Section 4 presents a comparison between the TM slowing down, typically observed prior a disruption, and the torque balance model of the interaction with the vacuum-vessel. Conclusions are drawn in Section 5.
In appendix A, the procedure adopted for tearing mode detection from edge magnetic probes is exposed. In appendix B, an analytical formula for the external radius of the island is derived.

2. Characterization of TM behavior by magnetic analysis

RFX-mod is equipped with a network of out-vessel magnetic pick-up sensors that are used for diagnosing integrated equilibrium and slow MHD phenomena [6]. As the vessel (made of Inconel) time constant amounts to few ms, the out-vessel signals are not well suited for fast MHD: to this purpose, the *Integrated System of Internal Sensors* (ISIS) was installed in RFX-mod [7, 8]. This diagnostics system includes several arrays of toroidal, poloidal and radial magnetic probes, installed on the inner surface of the vacuum vessel ($r_w = 0.475m$). The sampling frequency is 2 MHz and the estimated bandwidth is up to 500 kHz.
The amplitude and frequency of the time fluctuating components of the magnetic field, as well as their mutual phase relation, can be extracted from the edge probe signals. It is worth to note that signals provided by ISIS do not undergo any analog integration, but they provide the temporal derivative (through flux variation) of the magnetic field. In particular, the time derivative of poloidal and radial magnetic field components are measured by means of two poloidal arrays of 8 equally spaced coils each. The time derivative of the toroidal magnetic field fluctuations is, instead, measured by means of two arrays of 48 coils each, located at two opposite poloidal positions and uniformly distributed along the whole toroidal angle. Such a probe distribution was mainly designed to identify the wide $(1, n)$ MHD spectrum of the RFP configuration.
The identification of a given mode with poloidal and toroidal numbers (m, n), in terms of amplitude and phase, is made through a combination of Fourier analyses both in space and time domain. The procedure sequence is described in detail in Appendix A.

2.1. Tearing mode dynamics in circular tokamak discharges

In figure 1, two examples of the time behavior of the frequency spectra of the $m = 2, n = 1$ component is presented, along with the temporal evolution of I_p (ii) and $q(a)$ (iii), for two typical RFX-mod circular plasma discharges. As can be seen, the $m = 2, n = 1$ TM is rotating with a frequency of about 4.5 kHz during the plasma current flat-top phase, but, in the second case only (figure 1b), TM rotation slows down to about 0.5 kHz, after 550ms, and eventually the plasma disrupts. The disruption is identified by a spike in both safety factor and plasma current signals at $t \sim 620ms$. At the same time, the spectrogram shows a vertical band.

2.2. Consistency between in-vessel edge measurements and a vacuum cylindrical model

In this subsection we will show that the experimental estimates are consistent with a standard vacuum model in cylindrical geometry, which provides analytical expressions for the perturbed magnetic field components, in terms of modified Bessel functions [9]. In particular, the relationship between the fluctuating b_r and b_θ, as detected by the magnetic in-vessel probes, is consistent with the model prediction. The agreement, on one hand validates the analysis method of the magnetic signals; on the other hand

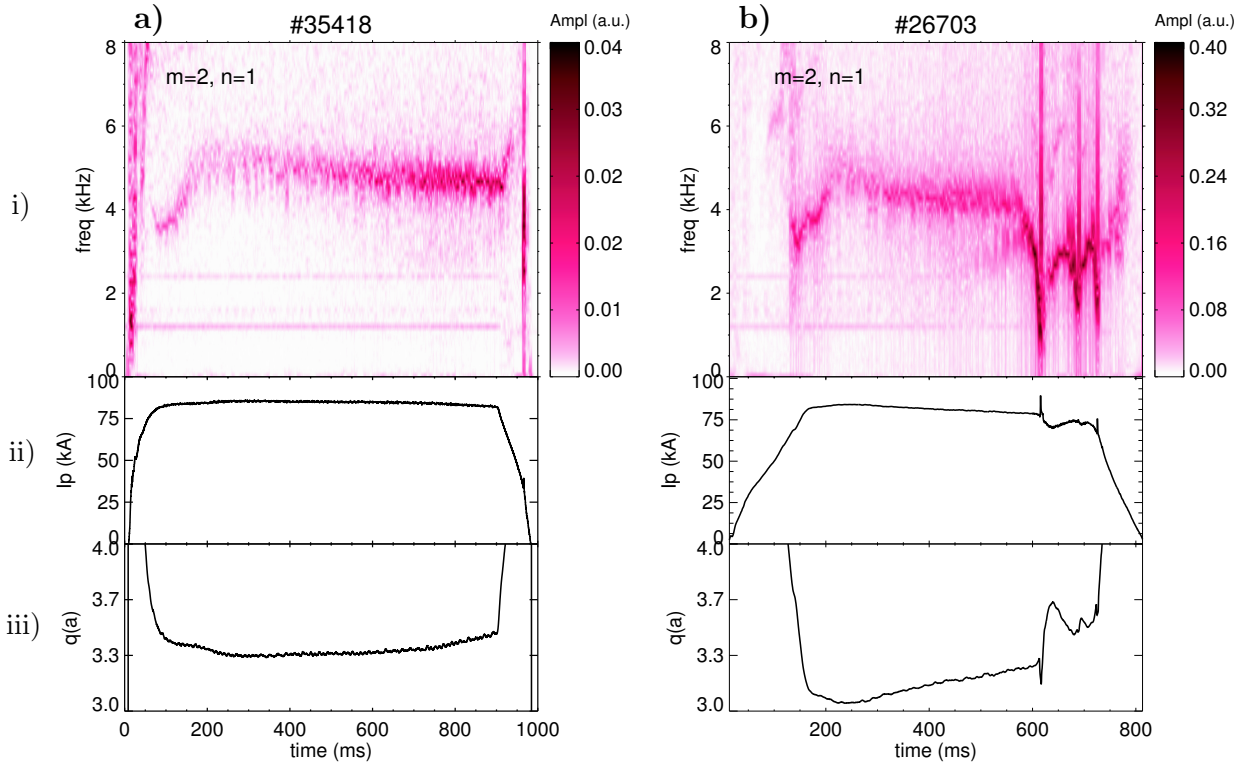

Figure 1. From top to bottom: i) spectrogram of $m = 2, n = 1$ magnetic fluctuations for a) #35418 and b) #26703 RFX-mod tokamak discharges, ii) time evolution of plasma current Ip and iii) edge safety factor q(a). A disruption occurred in shot #26703, identified by a current spike at time $t \simeq 620$ ms.

indicates that cylindrical geometry is a reasonable approximation when computing further quantities of interest, on the basis of edge measurements. In particular, we will extrapolate the measured b_r inside the plasma, thus providing an estimate of the island width associated to a resonant magnetic perturbation. The extrapolation is performed by solving Newcomb's equation, which gives the radial profile of the magnetic perturbation [2, 9], taking a suitable input for the magnetic equilibrium. Since Newcomb's equation is exactly the above mentioned vacuum representation outside the plasma, here we adopt the formalism of this equation for the sake of generality.

In the kHz frequency range we are dealing with, the screening of the vessel onto b_r is very important. This effect is included in the model as follows. The RFX-mod vacuum vessel is a complex three-dimensional structure made of Inconel 625, with a 2mm thick inner shell at the radius $r_w = 0.475$ m, and a 1mm thick outer shell at the radius $r_v = 0.505$ m [10]. The resistance in the poloidal direction differs from that in the toroidal direction due to anisotropic features. Therefore, the time-constant, which for a uniform shell would be the product of the vacuum permeability with the radius, the thickness and the conductivity, turns out to depend on the poloidal and toroidal mode numbers m, n of the perturbation. Gimblett's formula quantifies this effect for a thin shell [11], and provides a possible way to model the RFX-mod vessel: a single thin shell with the Gimblett's time constant [3] (poloidal and toroidal resistances are known quantities). For the mode numbers here considered ($m = 2, 3$, $n = 1, 2$) the Gimblett's time constant is about 2.3 ms. Here we prefer to use a different approach, approximating the vessel by two uniform thin shells, the innermost placed at $r = r_w$, the outermost at $r = r_v$, with time constants, τ_w and τ_v respectively, in the role of fitting parameters of magnetic probe data. The fit is considered successful if such parameters turn out to be comparable to the actual time constants of the inner and outer shell of the vessel: $\tau_w \sim \tau_v \sim 1$ ms.

RFX-mod is also equipped with an outermost (radial position $b = 0.5125$ m) copper shell, acting as stabilizing structure against MHD perturbations. With a 100ms time constant, it can be approximated as an ideal wall in the kHz frequency range we are analyzing. Hence, b_r is considered zero there.

Now we introduce the Newcomb's equation formalism. The solution of this equation gives the radial profile of the m, n Fourier harmonic of b_r (referred to the basis $e^{i(m\theta - n\phi)}$). Let's consider a resonant mode, i.e. suppose that a radius r_s exists inside the plasma where the safety factor q_{cyl} takes the value m/n. It is convenient to expand the b_r profile making use of a basis $\hat{\psi}_s(r)$, $\hat{\psi}_w(r)$, $\hat{\psi}_v(r)$ of real, independent solutions of Newcomb's equation:

$$-irb_r^{m,n} \equiv \psi^{m,n}(r,t) = \psi_s(t)\hat{\psi}_s(r) + \psi_w(t)\hat{\psi}_w(r) + \psi_v(t)\hat{\psi}_v(r) \tag{1}$$

The superscript m, n in the r.h.s have been dropped for ease of notation. The solution $\hat{\psi}_s(r)$ is regular at $r = 0$, equal to 1 at the mode resonant surface r_s, equal to 0 at $r \geq r_w$; the solution $\hat{\psi}_w(r)$ is 0 at $r \leq r_s$, 1 at r_w, 0 at $r \geq r_v$; the solution $\hat{\psi}_v(r)$ is 0 at $r \leq r_w$, 1 at r_v, 0 at $r \geq b$. Accordingly, the complex coefficients $\psi_s(t), \psi_w(t), \psi_v(t)$ encapsulate

amplitude and phase of the perturbation respectively at the resonant surface, at the innermost vessel surface and at the outermost vessel surface, respectively. For a non-resonant mode, Equation (1) is still valid letting $r_s = 0$ and $\psi_s(t) = 0$.
The radial function $\psi^{m,n}$ is everywhere continuous, but in general its first derivative has a discontinuity at r_s, r_w, r_v, modelling the presence of localized currents therein. Those at r_w, r_v rule the diffusion of the radial field across the vessel. To this purpose, the thin-shell dispersion relation $\tau_x \partial\psi^{m,n}/\partial t \equiv [r\partial\psi^{m,n}/\partial r]_{r_x-}^{r_x+}$ (being $x = w, v$) is taken into consideration: by exploiting (1), one gets

$$i\omega\tau_w\psi_w = E_{sw}\psi_s + E_{ww}\psi_w + E_{vw}\psi_v \tag{2}$$

$$i\omega\tau_v\psi_v = E_{wv}\psi_w + E_{vv}\psi_v \tag{3}$$

where $\omega = 2\pi f$, with f the mode frequency. The real coefficients $E_{yx} = rd\hat{\psi}_y/dr\Big|_{r_x-}^{r_x+}$ encapsulate the derivative discontinuities of $\hat{\psi}_y(y = s, w, v)$ at $r = r_x(x = w, v)$. It must be also taken into account that in vacuum [9]

$$b_\theta^{m,n} = -\frac{m}{m^2 + n^2(r/R_0)^2}\frac{\partial}{\partial r}\psi^{m,n} \tag{4}$$

From (1)-(4), the (complex) ratio between the m, n harmonics of poloidal and radial field, taken on the inner surface of the vessel, where the magnetic sensors are located, is

$$\left.\frac{b_\theta^{m,n}}{ib_r^{m,n}}\right|_{r_w-} = -\frac{m}{m^2 + n^2(r_w/R_0)^2}[A(\omega) + iB(\omega)] \tag{5}$$

with

$$A(\omega) = \frac{E_{vw}E_{wv}E_{vv}}{\omega^2\tau_v^2 + E_{vv}^2} - r_w \left.\frac{d\hat{\psi}_w}{dr}\right|_{r_w+}, \quad B(\omega) = \omega\left(\tau_w + \frac{E_{vw}E_{wv}}{\omega^2\tau_v^2 + E_{vv}^2}\tau_v\right) \tag{6}$$

All the parameters E_{yx} in (6), as well as $d\hat{\psi}_w/dr\Big|_{r_w+}$, refer to the vacuum region, hence they do not depend on plasma equilibrium. Quantities A, B very weakly depend on the mode numbers m, n. Therefore, the phase difference between b_r and b_θ is almost the same function of ω for different modes, and tends to $\pi/2$ for $\omega \to 0$.
For the mode here considered ($m = 2, 3$, $n = 1, 2$) one gets: $E_{vw} \sim E_{wv} \sim 16$, $d\hat{\psi}_w/dr\Big|_{r_w+} \sim -16$, $E_{vv} \sim -84$. Therefore the dependence of the coefficients A, B on τ_v turns out to be very weak. Instead, they are much more sensitive to τ_w. Accordingly, the comparison between the predictions of equation (5), (6) and the fluctuating b_r, b_θ extracted from magnetic coils, selects a very narrow interval for τ_w: $\tau_w \sim 1.1 - 1.3ms$. Instead, as far as τ_v is concerned, any value smaller than $4 - 5ms$ can be taken (hence, also $\tau_v = 0$). In figures 2, 3 specific examples are provided for a couple of shots, featuring a different equilibrium. In shot 35364 we have $q_{cyl}(a) \sim 3$, and the dominant perturbation pertains to the $m = 2, n = 1$ tearing mode. Its toroidal non-resonant sideband $m = 3, n = 1$ is also analyzed. In this shot, we take $\tau_w = 1.2$ ms and $\tau_v = \tau_w/2$. In shot 34642, the $m = 2$, $n = 1$ perturbation is replaced by the $m = 3$, $n = 2$ tearing mode, being $q_{cyl}(a) \sim 1.75$ (in RFX-mod the condition $q_{cyl}(a) < 2$ can be safely achieved thanks to the suppression of the non-resonant $m = 2$, $n = 1$ resistive

wall mode, by means of a sophisticated magnetic feedback system [12]). In this case we take $\tau_w = 1.1$ms, alongside $\tau_v = \tau_w/2$. The nearly coincidence of the chosen values of τ_w with the actual time constant of the inner shell indicates that the latter represents the most important screening component of the vessel. Nonetheless, the slight discrepancy between the best fitting τ_w for the $m = 2, n = 1$ and the $m = 3, n = 2$ modes could be symptomatic of the 3D structure of the vessel. However, the detection of the $m = 3$,

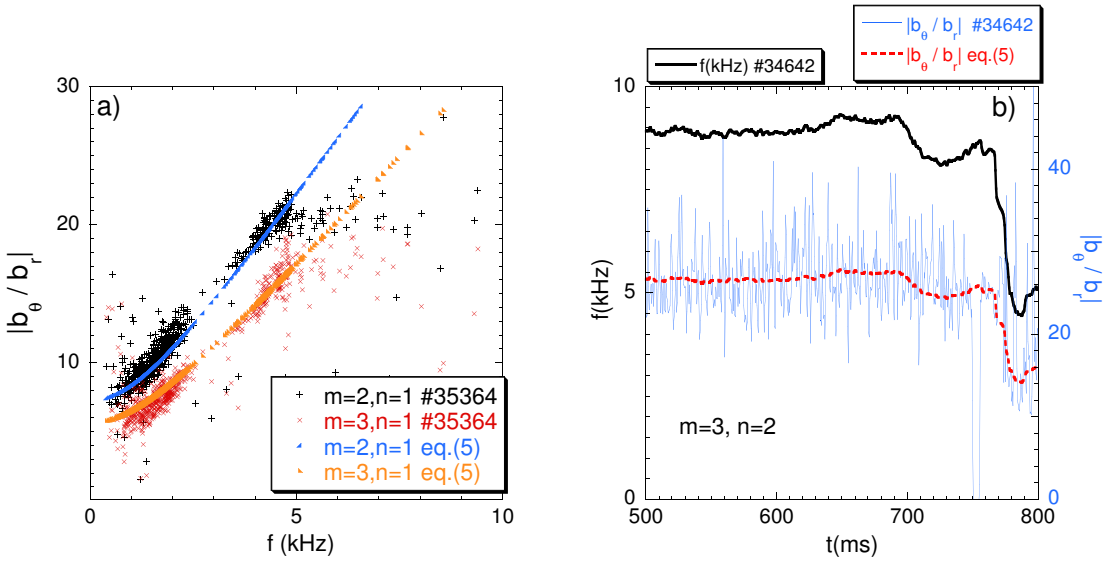

Figure 2. Ratio between the poloidal and radial field harmonics amplitudes. a) Experimental data from shot 35364 for tearing mode $m = 2, n = 1$ and its toroidal sideband $m = 3, n = 1$, vs mode frequency, alongside prediction from equation (5); in this shot, the mode slows down from $f \sim 4$kHz to $f \sim 2$kHz in the second half of the discharge. b) Experimental data from shot 34642 for tearing mode $m = 3$, $n = 2$, plotted as function of time, alongside prediction from equation (5); in this shot the mode slows down from $f \sim 9$kHz to $f \sim 5$kHz in the final part of the discharge.

$n = 2$ mode is not as reliable as that of the $m = 2$, $n = 1$, owing to its very small amplitude. Note, indeed, that the experimental data for this mode are rather scattered. Figure 2a shows that the ratio $|b_\theta/b_r|$ increases with f, due to the screening of the vessel onto the radial field. Figure 3 shows that the phase difference between b_θ and b_r, which is decreasing as a function of f, is insensitive to the mode number. In conclusion, a good consistency between the model and the edge magnetic data is obtained with realistic values of τ_w and τ_v. This result suggests that the magnetic data can be integrated within the model to extrapolate the magnetic perturbation inside the plasma. In particular, this allows an estimate of the TM island width, as discussed later on.

2.3. Extrapolation of the in-vessel edge measurements inside the plasma

The combination of equations (1) and (4), taken at $r = r_{w-}$ where edge magnetic measurements $b_{r,edge}$ and $b_{\theta,edge}$ for the m, n mode are provided, gives the radial field

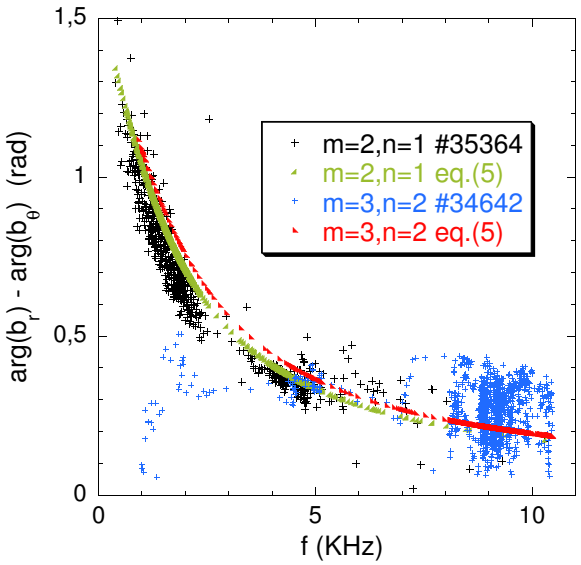

Figure 3. Phase difference between radial and poloidal field harmonics as function of frequency: experimental data from shot 35364 for harmonic $m = 2$, $n = 1$ and from shot 34642 for harmonic $m = 3$, $n = 2$, alongside prediction from equation (5).

amplitude and phase at the resonant surface, namely the quantity $\psi_s(t)$, as follows:

$$\psi_s = K b_{\theta,edge} + i H b_{r,edge} \tag{7}$$

$$K = \frac{m^2 + n^2 (r_w/R_0)^2}{m} \frac{r_w}{E_{sw}} , \qquad H = \frac{r_w}{E_{sw}} \left(E_{ww} - r_w \frac{d\hat{\psi}_w}{dr}\Big|_{r_w+} \right) \tag{8}$$

The coefficients E_{ww}, E_{sw}, hence K and H, are equilibrium-dependent. They are computed from the solution basis (1) of the zero-pressure Newcomb's equation. Neglecting pressure is a reasonable approximation for the ohmic plasmas of RFX-mod. Accordingly, the equilibrium is modelled by the standard current profile for the low-β tokamak [13]: $\mu_0 \mathbf{J} = \sigma \mathbf{B}$, with $\sigma(r) = \sigma_0 \left[1 - (r/a)^2\right]^\nu$, $\sigma_0 = 2/[q_{cyl}(0) R_0]$, $\nu \sim q_{cyl}(a)/q_{cyl}(0) - 1$. Therefore, only the two parameters $q_{cyl}(a), q_{cyl}(0)$ are required as input. The first is set by $q_{cyl}(a) = 5a^2 B_\Phi / [R_0 I_p(MA)]$. As far as $q_{cyl}(0)$ is concerned, independent estimates from internal inductance and on-axis Ohm's law display a linear trend with $q_{cyl}(a)$, as shown in [6]. Here, we adopt the linear interpolation $q_{cyl}(0) \sim 0.136 + 0.356 q_{cyl}(a)$. The amplitude $|\psi_s|$ so obtained is used to estimate the width of the magnetic island associated to the resonant mode. This is the topic of the next subsection.

2.4. Estimate of the island width

According to a standard text-book formula the 'nominal' island width W is given by the mode amplitude at the resonant surface divided by an equilibrium related coefficient

[9]:

$$W = 4\left(\left|\frac{\psi_s}{dF_0(r_s)/dr}\right|\right)^{\frac{1}{2}}, \qquad F_0(r) \equiv mB_\theta - nB_\phi r/R_0 \tag{9}$$

It is implicit that the perturbed quantities refer to the m, n harmonic. We speak of 'nominal' width since (9) is valid under the so-called 'constant-ψ approximation', i.e. when $\psi^{m,n}$ weakly varies within the island. For macroscopic islands this assumption is not justified, in particular for the $m = 2, n = 1$ mode. In such cases, the island width can be estimated only from the reconstruction of the magnetic topology as obtained, for example, by a field line tracing code. Nonetheless, for high-frequency $m = 2, n = 1$ and $m = 3, n = 2$ tearing modes, at $r \geq r_s$, the radial function $|\psi^{m,n}|$ can be approximated by a linear decreasing function vanishing at the vessel inner surface r_w. In such a case, a refinement, as far as the maximum 'external' radial excursion of the island is concerned, can be straightforwardly found: in appendix B it is shown that the point on the island separatrix corresponding to the maximum radius is

$$r_{island,ext} = r_s + \frac{W}{2} - \frac{W^2}{16(r_w - r_s)} \tag{10}$$

Formula (10) improves the 'constant-ψ expression' $r_{island,ext} = r_s + W/2$. Finding a similar equation for the *inboard* side of the island, which combined with (10) would give the *true* island width, does not seem an easy task, due to the non-monotonic, strongly equilibrium-dependent behavior of $|\psi^{m,n}|$ for $r \leq r_s$.

For the sake of clarity, we want to underline here that the validity interval of the Newcomb's equation, which gives an estimate of the perturbation profile $b_r^{m,n}(r)$, must not be superimposed on that of the Rutherford's equation, $W/a << 1$, which gives an estimate of the island width time-evolution. We do not employ the Rutherford's equation in the present analysis. Newcomb's equation derives from the linearized ideal-MHD force balance constraint $\nabla \times (\widetilde{\mathbf{j}} \times \mathbf{B}_0 + \mathbf{J}_0 \times \widetilde{\mathbf{b}} = 0)$. Therefore, this equation is valid as long as $\widetilde{b}/B_0 \ll 1$. Rutherford's and Newcomb'e equations have different limits of applicability. Let's consider the 'standard' island width formula (9)

$$W = 4\left(\left|\frac{\psi_s}{F_0'(r_s)}\right|\right)^{\frac{1}{2}} \rightarrow \frac{W}{a} \sim 4\left(\frac{R_0}{a}\right)^{\frac{1}{2}}\left(\left|\frac{b_r(r_s)}{B_\phi}\right|\right)^{\frac{1}{2}} \sim 8\left(\left|\frac{b_r(r_s)}{B_\phi}\right|\right)^{\frac{1}{2}}$$

where the approximation holds for the $m = 2, n = 1$ mode in RFX-mod. This formula clarifies that a macroscopic island, for which the Rutherford's equation description is doubtful, is associated to a relatively small magnetic perturbation. For example, taking $W/a = 0.5$, we get $b_r(r_s)/B_\phi \sim 0.4\%$. In this conditions Newcomb's equation is still applicable.

An example of W estimate for the $m = 2, n = 1$ mode is shown in figure 4a (black continuous line), where the growth of a large island ($W/a > 0.5$), associated to a slowing down of the mode, eventually triggers a disruption ($t = 530$ms).

A similar evaluation, based on the out-vessel sensors (black dotted line), is affected by the vessel screening, thus giving a comparable, but smaller result. The growing mode

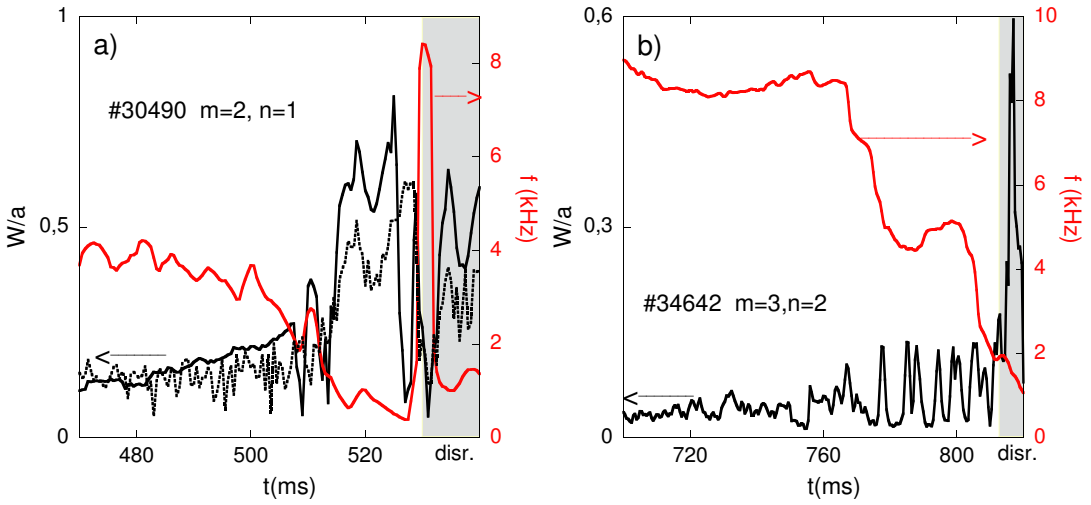

Figure 4. Estimates of the normalized island width W/a, from in-vessel edge measurements (black continuous line) and from out-vessel probes (black dotted line), the latter limited to plot a). Mode frequency, from in-vessel edge measurements, is shown in red. The disruptive phase is shaded in gray. Plot a) displays the $m = 2$, $n = 1$ mode for shot 30490: in the examined interval, $q_{cyl}(a) \sim 3$ and the Greenwald normalized density is $n_e/n_G \sim 0.75$. Plot b) displays the $m = 3$, $n = 2$ mode for shot 34642: in the examined interval, $q_{cyl}(a) \sim 1.8$, and $n_e/n_G \sim 0.2$.

slows down during the pre-disruptive phase, from $f \sim 4$kHz to $f \sim 0.4$kHz, without locking to the wall in the strict sense (the following frequency spike occurs during the disruption).

A similar W estimate for the $m = 3, n = 2$ mode is shown in figure 4b. The maximum island width prior to the disruption, $W/a < 0.15$, is smaller than the typical disruptive values of the $m = 2, n = 1$ island (the following spike of W takes place during the disruption process). The disruption occurs after a slowing down of the mode from $f \sim 8$kHz to $f \sim 2$kHz.

A growing amplitude, slowing down TM is the signature of the majority of the disruptions observed in the RFX-mod tokamak. Regardless of the fact that TM is or not the original cause of the disruption, it surely takes a part in the final process. Therefore it is interesting to analyze the island width in the pre-disruptive phase of the discharge. This is the subject of the following subsection.

2.5. Disruptions analysis

A new statistical analysis over a database of discharges disrupted after a slowing down of the dominant tearing mode ($m = 2$, $n = 1$ or $m = 3$, $n = 2$) refines previously published results obtained from analysis with the outer magnetic sensors (figures 5-7 of [6]). Figure 5a confirms what was stated in [6]: the $m = 2$, $n = 1$ (nominal) island width prior to the disruption increases with $q_{cyl}(a)$. This trend is interpreted as due to

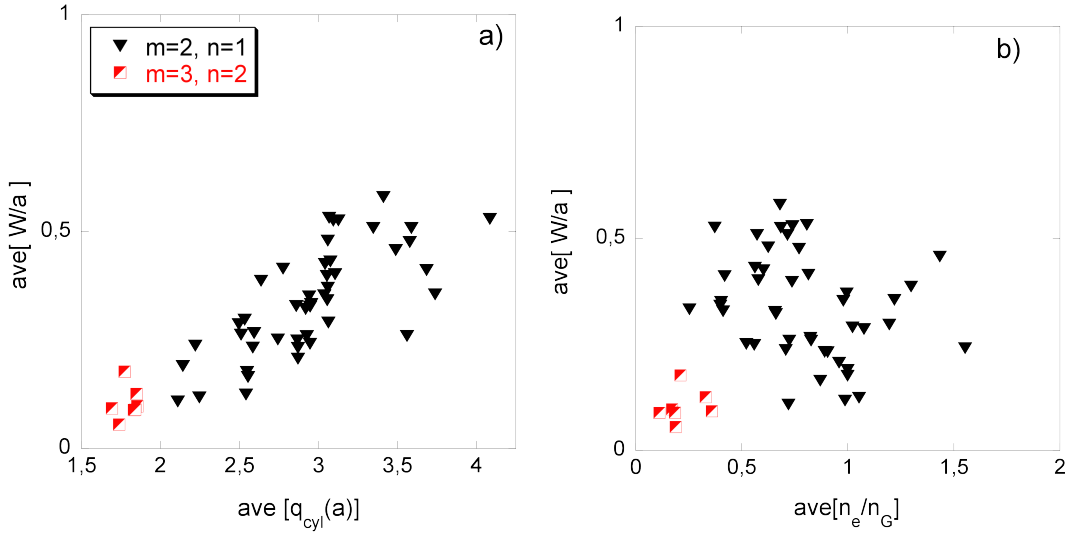

Figure 5. Statistical analysis on a database of disrupted discharges characterized by a slowing down of the dominant tearing mode. The average W/a is plotted against (a) the average edge cylindrical safety factor and (b) the average value of n_e/n_G . All quantities are estimated within $10 \div 20$ ms before the disruption.

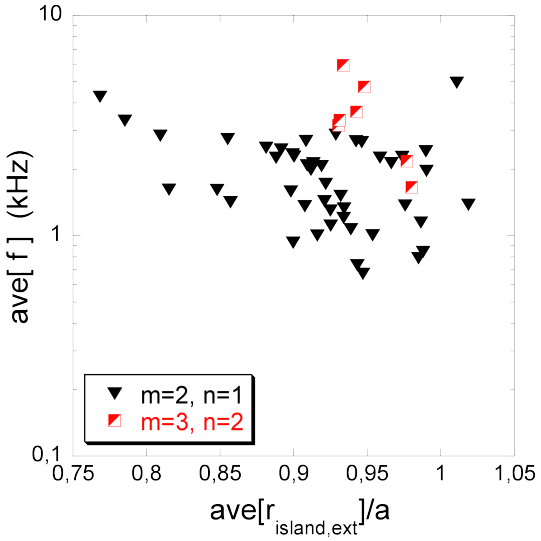

Figure 6. Analysis on the same shots considered in figure 5. The average frequency attained by the mode before the disruption is plotted against the average value of the outward island radius, as given by formula (10). Both quantities are estimated within $10 \div 20$ ms before the disruption. note the log scale for the y-axis.

the increase with $q_{cyl}(a)$ of the distance between the resonant surface, where the island develop, and the plasma-facing stabilizing structures (vacuum-vessel and shell). For the $m = 3$, $n = 2$ island the range of $q_{cyl}(a)$ is not wide enough to establish a clear trend. Note, in fact, that the amount of data relative to the $m = 3$, $n = 2$ is rather poor.
Figure 5b shows that, at least for the examined cases, the $m = 3$, $n = 2$ induced

disruptions occur at W/a and n_e/n_G smaller than those featuring the $m = 2, n = 1$ disruptions. Nonetheless, according to figure 6, the external radius of the island, as given by equation (10), gets close or even beyond the plasma surface, in both cases. The figure reports also the minimum rotation frequency of the island, observed before the disruption: in fact, this quantity is better correlated with the external radius of the island, which combines both equilibrium and W, than with W alone.
Note that, none of the considered cases is wall-locked. Disruptions with a true wall-locked $m = 2, n = 1$ TM also occur in RFX-mod, but only at $q(a)$ very close to 2. Nonetheless, the $q_{cyl}(a) \sim 2$ cases are more benign than those considered in the database, since they feature a relatively small island width (see trend of figure 5a), so they can be successfully managed (in general) by the magnetic feedback. The feedback action mitigates the wall-locking by inducing a slow rotation regime (about 50Hz), thus preventing the mode further growth related to the penetration of the passive structures, and avoiding the disruption [6]. With active coils outside the copper shell, the magnetic feedback can control the island width only indirectly, by keeping small the edge radial field amplitude. Therefore it cannot do much when W is large with an edge radial field already small because of the significant rotation, as in the high-frequency disruptions considered in the present database.

3. Interpretation of the tearing modes island rotation frequency

In this section, TM frequencies obtained from the in-vessel edge data are interpreted by means of a two-fluid phenomenological model, already used to describe the island fast rotation in the low-current RFP plasmas ($Ip \leq 100$kA) of RFX-mod [5]. A connection between TM island rotation, plasma flow and kinetic profiles is established by the model.

3.1. Two-fluids model of TM island rotation

The model formalizes the assumption that the magnetic island is frozen within the electron fluid at the resonant surface. This hypothesis is supported by experimental observation both in tokamak [4] and stellarator [14]. From a theoretical point of view, it is justified for small-size islands, unable to flatten significantly the pressure profiles at the resonant surface, whereas, above an amplitude threshold, the island should propagate with the ion fluid [15, 16]. Here we do not attempt any comparison between the amplitude threshold, as predicted by the mentioned works, and the island width, as estimated in RFX-mod.
Referring the harmonics to the basis $e^{i(m\theta - n\phi)}$, the electron-fluid frozen condition implies that the island phase velocity is a combination of the poloidal and toroidal angular velocities ($\Omega_\phi = V_\phi/R_0$, $\Omega_\theta = V_\theta/r$) of the electrons at the resonant radius:

$$\frac{d\varphi^{m,n}}{dt} = n\Omega_{\phi,e}(r_s,t) - m\Omega_{\theta,e}(r_s,t) = \left.\frac{n}{R_0 B_\theta}(\mathbf{B}\times\mathbf{V}_e)_r\right|_{r_s} \tag{11}$$

To get the last equality, the equation $q_{cyl}(r_s) = m/n = rB_\phi/(R_0B_\theta)|_{r_s}$ was used. Note

that only the velocity perpendicular to $\mathbf{B}$ contributes to (11). This equation is managed in order to express $\mathbf{V}_e$ in terms of the *total* ion velocity combined with the *diamagnetic components* of electron and ion velocities. The former can be indeed estimated by spectroscopic diagnostic, the latter by pressure profile reconstruction. Taking the perpendicular velocity, in the absence of any external momentum input, as the sum of the $\mathbf{E}\times\mathbf{B}$ drift and the diamagnetic drift, the total velocity for ions and electrons is:

$$\mathbf{V}_j = \mathbf{V}^{E\times B} + \mathbf{V}_j^{diam} + \mathbf{V}_j^{//} \; ; \qquad \mathbf{V}_j^{diam} = \pm\frac{1}{en_eB^2}\nabla p_j \times \mathbf{B} \; ; \quad (j=e,i) \tag{12}$$

where $\mathbf{V}_j^{//}$ represents the parallel velocity component. The diamagnetic velocity definition holds with sign + for electrons and − for ions. Symbol $e>0$ denotes the electron charge magnitude, n_e the electron density ($=n_i$), p_e, p_i the electron and ion pressure respectively.
The $\mathbf{E}\times\mathbf{B}$ drift is the same for electrons and ions. Therefore, the electron velocity is related to the ion velocity by:

$$\mathbf{V}_e = \mathbf{V}_i + \mathbf{V}_e^{diam} - \mathbf{V}_i^{diam} + \mathbf{V}_e^{//} - \mathbf{V}_i^{//} \tag{13}$$

By combination of (11) and (13), one ends up with the formula:

$$\frac{d\varphi^{m,n}}{dt} = \omega_{diam} + \omega_{flow} \tag{14}$$

$$\omega_{diam} = \frac{m}{en_erB_\phi}\frac{d(p_e+p_i)}{dr}\bigg|_{r_s} \; ; \qquad \omega_{flow} = n\Omega_{\phi,i}(r_s,t) - m\Omega_{\theta,i}(r_s,t) \tag{15}$$

The island phase velocity can be modelled by the sum of two terms taken at the resonant surface: a 'flow' frequency, associated to the ion velocity, and a 'diamagnetic' frequency, determined by pressure and density profiles. Note that ω_{flow} is the frequency of an island frozen within the ion-fluid. An expression similar to (14) has been derived within a two-fluid model of the error field penetration [17].
An estimate of r_s is needed to implement (14). Despite the lacking in RFX-mod of a specific diagnostic for a direct measurement of $q(r)$, this can be obtained by equilibrium reconstructions. Here, we make use of the toroidal version, with the same input parameters, of the cylindrical equilibrium model described in subsection 2.3. The latter adapts the method developed for the RFP [18] to the circular cross section, low-β tokamak.

3.2. Evaluation of ω_{diam}

The diamagnetic frequency is obtained by estimates of density and temperature radial profiles. Electron and ion densities are equal ($n_i = n_e$), since only hydrogen and deuterium plasmas are analyzed. The electron density profile is computed by inversion of the interferometer data [19], using a numerical code exploiting flux coordinate [20]. The electron temperature profile is resolved by means of a Thomson scattering diagnostic

[21], measuring T_e at 78 radial positions, with a spatial resolution of about 1 cm. The following interpolating profile is adopted:

$$T_e(r) = T_0 \left(1 - \left(\frac{r}{a}\right)^{\alpha}\right)^{\beta} + T_{edge} \tag{16}$$

While α, β, T_0 are fitting parameters, the edge temperature T_{edge} is determined by the triple Langmuir probes located at the vacuum vessel radius. In fact, these probes represent a useful complementary diagnostic for the outermost region of the plasma, where the Thomson scattering data are not available or unreliable. A good reconstruction of T_e in this region is mandatory to estimate ω_{diam} when r_s gets close to a. Figure 15b presents an example of the temperature measured by the Thomson scattering, alongside the fitting profile (16). Note that the $m = 2$, $n = 1$ resonant radius (highlighted by a vertical line) is outside the region covered by the Thomson scattering, in this particular shot. Hence, the necessity of including the Langmuir probes data in (16) for fitting T_e profile.

In RFX-mod the ion temperature T_i can be estimated by the Neutral Particle Analyzer [22] but this measurement is not available in the shots analyzed in this paper. It is found that, in similar discharges, $T_i \sim 2/3 T_e$ on average. Therefore, we assume $T_i(r) = 2/3\, T_e(r)$ with profile (16). For both density and temperature, the profiles are reconstructed every 10ms, according to the sampling time of the relative measurements. Let us note that temperature and density measurements were available on a limited subset of the discharges, due to the fact that these diagnostics were designed for RFP plasma conditions.

3.3. Comparison between ω_{diam} and magnetic frequencies

We present, in this subsection, the comparison between the frequencies obtained by the magnetic probes (hereinafter dubbed 'magnetic frequencies') and the ω_{diam} frequencies predicted by the model, described in Equation (15). At the moment, we do not consider in the comparison the contribution of the ω_{flow} term, which will be reported later by the subsection 3.4. We want to demonstrate that the diamagnetic term represents the main contribution in determining the rotation frequency of the mode.

First, we consider shot 35372, whose equilibrium parameters are displayed in figure 7: it is a $q_{cyl}(a) \sim 2.5$ discharge featuring both $m = 2$, $n = 1$ and $m = 3$, $n = 2$ modes, as can be seen in the spectrogram obtained from the magnetic signals (panel i). The comparison with the ω_{diam} term is performed only in the time interval [135, 245]ms, where both electron density and temperature are available. But, as far as the $m = 3$, $n = 2$ mode is concerned, it is further restricted to the sub-interval [205, 245]ms, where mode amplitude can be detected with sufficient accuracy. Referring to these time intervals, figure 8 shows the magnetic frequencies and the ω_{diam} ones, deduced from the model. The colored bands represent the error estimate. A negative frequency means that the island moves in the electron diamagnetic direction. Note that a quite good agreement is found, for both the $m = 2$, $n = 1$ and $m = 3$, $n = 2$ modes.

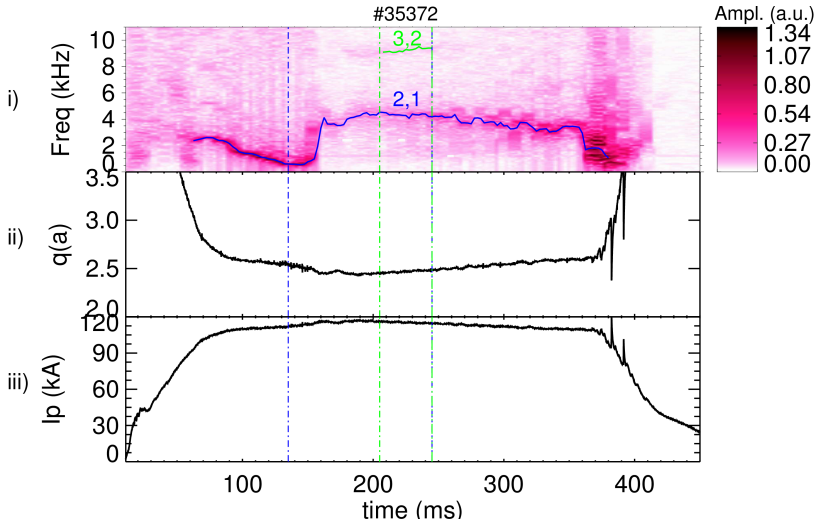

Figure 7. i) Spectrogram of edge magnetic fluctuation data for discharge 35372 . The $m = 2$, $n = 1$ and $m = 3$, $n = 2$ mode frequencies are highlighted. ii) Time traces of edge safety factor $q_{cyl}(a)$ and iii) plasma current I_p. The vertical lines identify the time intervals where the comparison with model (14) is done.

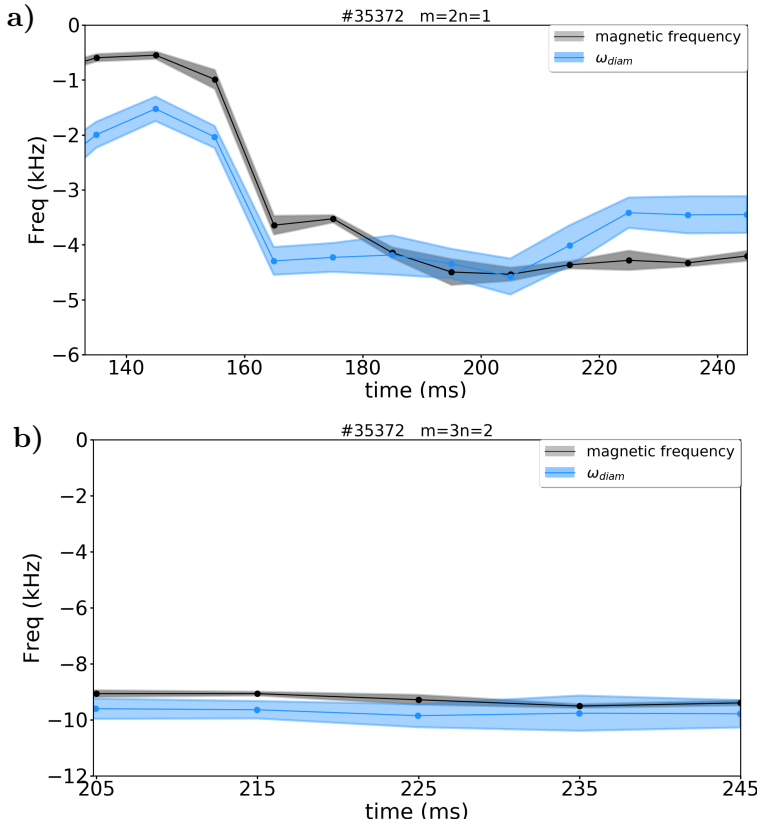

Figure 8. Comparison of TM magnetic frequencies (black) and the diamagnetic component ω_{diam} (blue) of model (14). Panel (a) refers to the $m = 2$, $n = 1$ TM, panel (b) to the $m = 3$, $n = 2$ TM. The estimated error is represented by the colored bands.

Accordingly, the $m = 2, n = 1$ spin up at about 150ms (see figure 9a) is due to a modification of ω_{diam}. From figure 7, one can see that no significant modification of the magnetic equilibrium can explain such a spin-up. Further evidences of this strict correlation between the 'magnetic' and the diamagnetic frequencies will be provided in the following.

3.4. Evaluation of ω_{flow}

We now add the ω_{flow} term to have a complete comparison between the experimentally determined magnetic frequencies and those predicted by model (14).
In RFX-mod, ion velocity is estimated by means of a multi-chord Doppler spectroscopy diagnostic, which measures impurity emissions, integrated over several poloidal and toroidal lines of sight [23]. The spectrum is acquired for three different ions: CIII ($\lambda = 4647$ Å), CV ($\lambda = 2271$ Å) and OV ($\lambda = 6500$ Å). It should be considered that the diagnostics does not allow reconstructing the radial profile with the resolution necessary to estimate the velocity at the resonant surface, as required by (15). However, this is not a strong limitation in the present analysis, since the ω_{flow} term only moderately participates in determining the TM island rotation, as this is dominated by the ω_{diam} contribution, as will appear clear from section (3.4.2.1)
For the best estimation of ω_{flow} term, we will model the toroidal and poloidal flow components with reasonable assumptions. In particular, for the poloidal flow, we rely on two different models. The first uses a phenomenological poloidal flow damping term (subsection 3.4.2), the second one is based on neoclassical theory (subsection 3.4.3).

3.4.1. Evaluation of toroidal velocity profile

For the toroidal flow component, we take the following model profile, which is given by the toroidal component of the single-fluid (i.e. ion) MHD motion equation in stationary conditions [24]:

$$\frac{1}{r}\frac{d}{dr}\left(\mu\, r \frac{d}{dr}\Omega_{\phi,i}\right) + S_\phi = 0 \tag{17}$$

Here μ is the perpendicular viscosity and S_ϕ is the *phenomenological* momentum source density, considered radially constant for the sake of simplicity. The velocity boundary conditions, which satisfy on-axis continuity of the derivative and the constraint of small velocity at the plasma edge, are:

$$\frac{d}{dr}\Omega_{\phi,i}(0) = \Omega_{\phi,i}(a) = 0 \tag{18}$$

The solution of (17) satisfying (18) is:

$$\Omega_{\phi,i}(r) = \frac{S_\phi \tau_V}{4\rho}\left(1 - \frac{r^2}{a^2}\right) \tag{19}$$

The quantity $\tau_V = \rho a^2/\mu$ is the viscous diffusion time, being ρ the mass density. The latter equation can be rewritten as

$$\Omega_{\phi,i}(r) = \Omega_{\phi,i}(0)\left(1 - \frac{r^2}{a^2}\right) \tag{20}$$

where the global coefficient $\Omega_{\phi,i}(0)$ is here determined by the above mentioned spectroscopic measurement by assuming the same toroidal velocity for ions and impurities. This is justified for a collisional plasma [25], as that under discussion.

3.4.2. Phenomenological poloidal flow

The model considers the following poloidal component of the single fluid MHD motion equation in stationary condition [24]:

$$\frac{1}{r^3}\frac{d}{dr}\left(\mu\, r^3 \frac{d}{dr}\Omega_{\theta,i}\right) - \frac{\rho}{\tau_D}\Omega_{\theta,i} + S_\theta = 0 \tag{21}$$

The second term in (21) is phenomenological, and it models the poloidal flow damping, by assuming a characteristic time τ_D. In the framework of the cylindrical tokamak theory, this model has been adopted in [2]. The velocity boundary conditions, as for the toroidal flow case, are:

$$\frac{d}{dr}\Omega_{\theta,i}(0) = \Omega_{\theta,i}(a) = 0 \tag{22}$$

We assume all the quantities μ, ρ, τ_D, S_θ to be radially constant, as before. Then, the solution of (21) satisfying (22) is:

$$\Omega_{\theta,i}(r) = \frac{S_\theta \tau_D}{\rho}\left(1 - \frac{a}{r}\frac{I_1\left(\frac{r}{a}\sqrt{\frac{\tau_V}{\tau_D}}\right)}{I_1\left(\sqrt{\frac{\tau_V}{\tau_D}}\right)}\right) \tag{23}$$

where I_1 is the first-order modified Bessel function and the combination $\sqrt{\tau_V/\tau_D}$ represents a shape parameter for $\Omega_{\theta,i}(r)$. The latter equation can be written as:

$$\Omega_{\theta,i}(r) = \Omega_{\theta,i}(0)\frac{F(r)}{F(0)}\ , \qquad F(r) = \left(1 - \frac{a}{r}\frac{I_1\left(\frac{r}{a}\sqrt{\frac{\tau_V}{\tau_D}}\right)}{I_1\left(\sqrt{\frac{\tau_V}{\tau_D}}\right)}\right) \tag{24}$$

where, again, $\Omega_{\theta,i}(0)$ is determined by spectroscopic measurement, though main ion and impurities can have quite different poloidal velocities [25]. However, this is not a major issue, given the estimated small contribution of ω_{flow} with respect to ω_{diam}.

3.4.2.1. Model and experimental data comparison

In a first analysis we take $\tau_V = 60ms$ and $\tau_D = \tau_V/350$, considering that τ_V should be comparable to the energy confinement time, and that the observed strong damping of the spectroscopic poloidal velocity implies $\tau_D \ll \tau_V$ (by comparison between (19) and (23)).

The particular value chosen for the ratio τ_V/τ_D will be justified by a chi-square test (sensitivity analysis) between the modelled frequency and the frequency detected by the magnetic coils. In any case, the modelled frequency (14) weakly depends on these two characteristic times, as we shall see later on in subsection 3.4.2.2.
The figure 9 shows the comparison for shot 35372, together with the ω_{diam} and ω_{flow} components, as previously derived. A good agreement is found between the magnetic and modelled frequencies, for both the $m = 2, n = 1$ and $m = 3, n = 2$. It can be seen that the rapid change in frequency of $m = 2, n = 1$ mode at $t \sim 160$ ms is associated with the corresponding change in the diamagnetic component, while the flow component changes only slightly.

The same analysis has been performed on shot 33822, characterized by a $q_{cyl}(a) < 2$ phase (figure 10) where the $m = 3$, $n = 2$ amplitude becomes important. This mode appears earlier at 100ms with a frequency of about 8 kHz (see figure 10b), almost constant

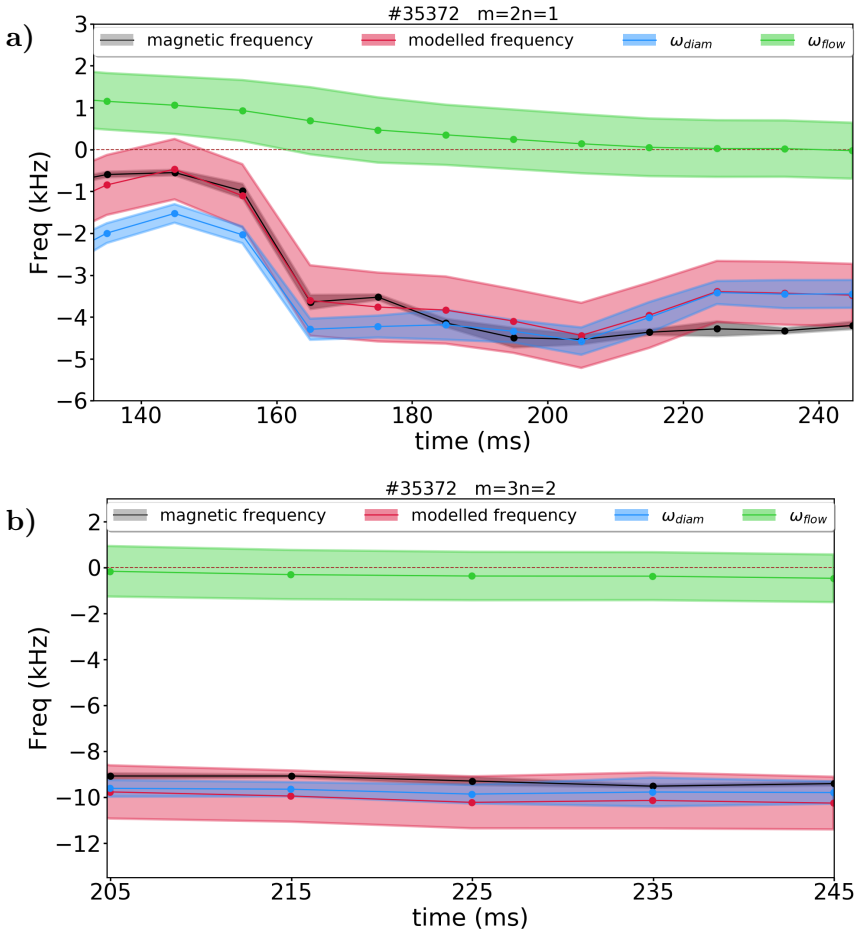

Figure 9. Comparison of TM magnetic frequencies (black) and the full modelled frequencies of (14). The components ω_{diam} and ω_{flow} are reported as well. Panel (a) refers to the $m = 2$, $n = 1$ TM, panel (b) to the $m = 3$, $n = 2$ TM. The estimated error is represented by the colored bands.

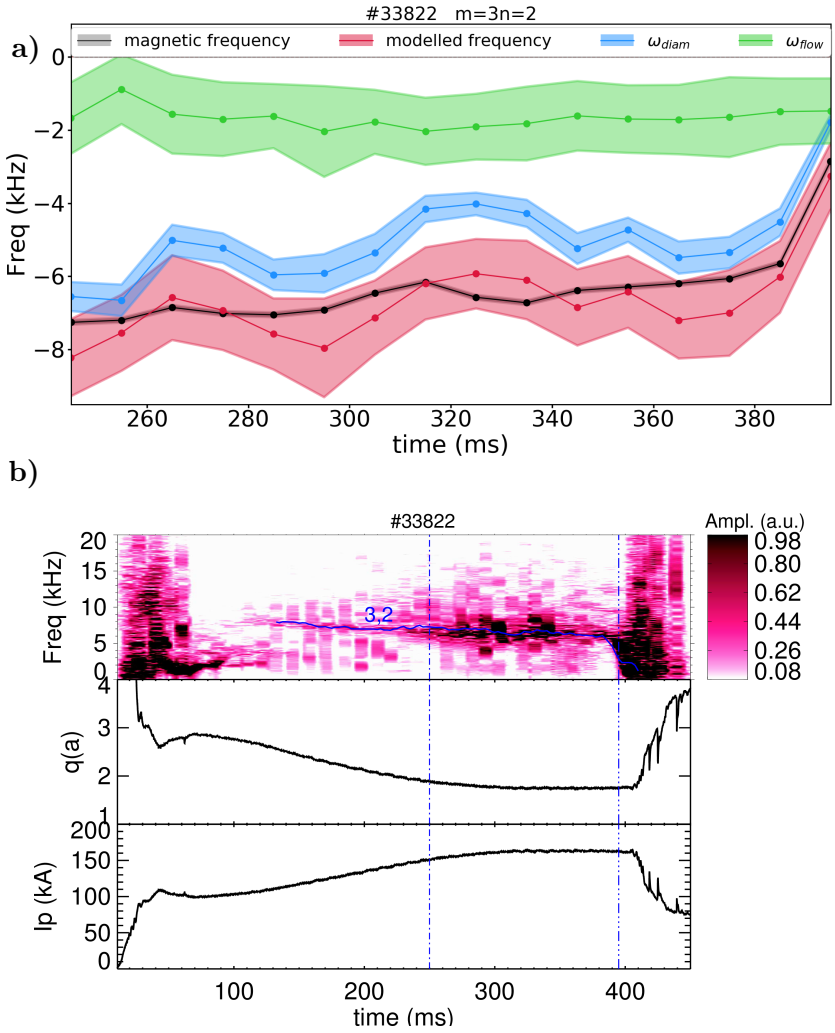

Figure 10. Analysis of the $m = 3, n = 2$ TM in shot 33822. a) Comparison of TM magnetic frequencies (black) and the full modelled frequencies of (14). The components ω_{diam} and ω_{flow} are reported as well. b) same quantities as in figure 7. The vertical lines identify the time interval where the comparison with the model is performed.

up to 375ms. Afterwards, it rapidly slows down to few hundreds Hz, and a disruption occurs. A good agreement between the magnetic and ω_{diam} frequencies is found even in this case, with the same dominance of ω_{diam} over ω_{flow} (see figure 10a). The final slowing down of the mode follows a quenching of ω_{diam}, whereas ω_{flow} does not exhibit significant variations. It is worth to mention that the present analysis differs from that presented in [26], which was dedicated to the study of the effect of 3D fields due to intrinsic magnetic field errors or active coils on the plasma flow in RFX-mod.

3.4.2.2. Analysis of the sensitivity on τ_V/τ_D

A justification for the above choice $\tau_V/\tau_D = 350$ is given by a chi-square test: for several values of τ_V/τ_D, the quantity $\chi^2(\tau_V/\tau_D)$ is computed as the sum of the sampled squared

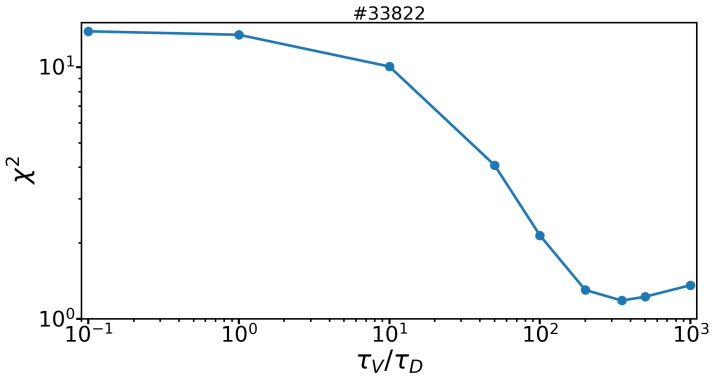

Figure 11. Chi-square parameter as a function of τ_V/τ_D for shot 33822. A minimum is obtained for $\tau_V/\tau_D \approx 350$.

differences between the modelled and magnetic frequencies, weighed by the error on the modelled frequency (the error on the magnetic frequency is much smaller, it is thus neglected). In Figure 11 such χ^2 is plotted for the shot 33822 in a wide range of τ_V/τ_D, which covers four orders of magnitude: a minimum is obtained for $\tau_V/\tau_D \approx 350$, representing the best agreement between modelled and magnetic frequencies. The explicit comparison is shown in figure 12 for the considered extreme values of τ_V/τ_D. Only a weak dependence turns out on this parameter, in the large interval explored, in agreement with the previous consideration that ω_{flow} is a minor contribution within the modelled frequency.

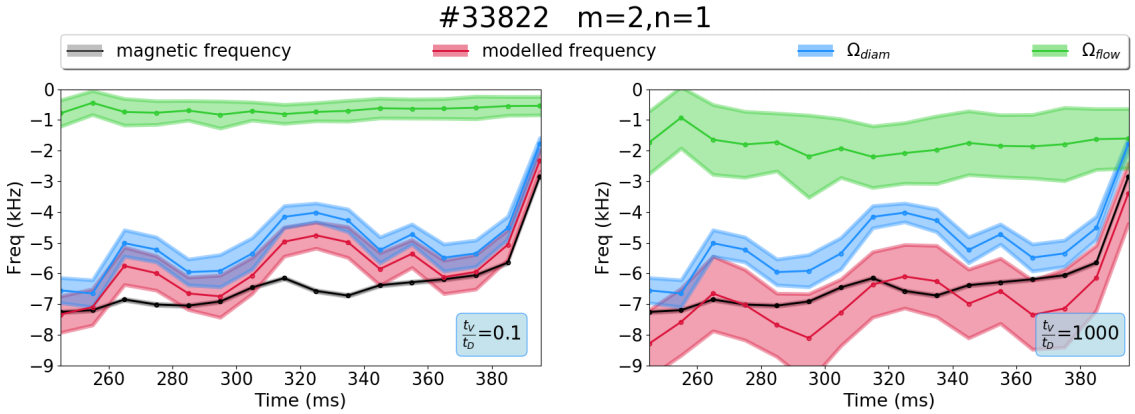

Figure 12. Comparison between the magnetic and modelled frequencies (the latter reported with the diamagnetic and flow components) for two extreme values of τ_V/τ_D as in figure 11. Note that, as expected, ω_{flow} varies with this ratio, whereas ω_{diam} does not.

3.4.3. Neoclassical poloidal flow model

The customary model for the poloidal flow velocity makes use of neoclassical calculation as described in [25]. Neoclassical poloidal flow of the main ions, largely driven by the

temperature gradient, is described by eq. (33) in [25]. A simplified version of such formula, by considering $B \sim B_\phi$, is:

$$V_\theta^i(r) \approx k_1 \frac{1}{B} \frac{dT_i}{dr} \tag{25}$$

where k_1 is a function of collisionality and the superscript i denotes that we are referring just to the main ion.

We use this relation, considering $T_i(r) = 2/3T_e(r)$, to estimate the poloidal velocity in our model by optimizing the parameter k_1. As before, this χ^2 analysis is based on the discrepancies between the modelled and magnetic TM frequencies for the same shot 35372 as in figure 9. The result of this analysis is presented in figure 13. It turns out that the best agreement is found for $k_1 \approx 0.25$. This k_1 value implies a low poloidal flow velocity ($\sim 400 m/s$) which is not surprising taking into account that the ω_{diam} term is already in a good agreement with the experimental data.

As predicted by theory, k_1 is a function of the ion collisionality ν_i^*, defined as the ratio of ion-ion collision frequency to bounce frequency $\nu_i^* = \nu_{ii} R_0 q (R_0/a)^{3/2} v_{th,i}$, and the impurity strength parameter $\alpha = n_I Z_I^2 / n_i Z_i^2 = \frac{Z_{eff}-1}{1-Z_{eff}/Z_I}$, where the subscripts i and I represent the primary ion and impurity species, with the assumption of single impurity species; Z_i, Z_I, Z_{eff} are the main ion charge, impurity charge and effective charge respectively, respectively.

A typical value for ν_i^* can be estimated for the RFX-mod tokamak plasma. In cylindrical approximation and introducing the Greenwald density $n_G = I_p[MA]/(\pi a^2)$, one gets $\nu_i^* \approx 5.5 \times 10^{-4} \ln\Lambda \frac{B_t}{I_p} (\frac{R_0}{a})^{\frac{3}{2}} \frac{n}{n_G} T_i^{-2}$. The considered shot 35372 is characterized by $T_i \sim 0.23 keV$, $I_p \sim 0.12 MA$, $n/n_G \sim 0.55$ and $\ln\Lambda \sim 17$, hence ν_i^* is about 3.7.

As far as α is concerned, in the expected range $Z_{eff} < 2$ (no Z_{eff} measurement is possible in these plasmas, but they should be relatively clean, due to the frequent use of glow-discharges cleaning and low input power), and assuming carbon impurity with $Z_I = 6$, one would get $\alpha < 1.5$. On the basis of these estimates for ν_i^* and α, the optimum $k_1 = 0.2$ is compatible with the theoretical prediction of figure 1 of [25].

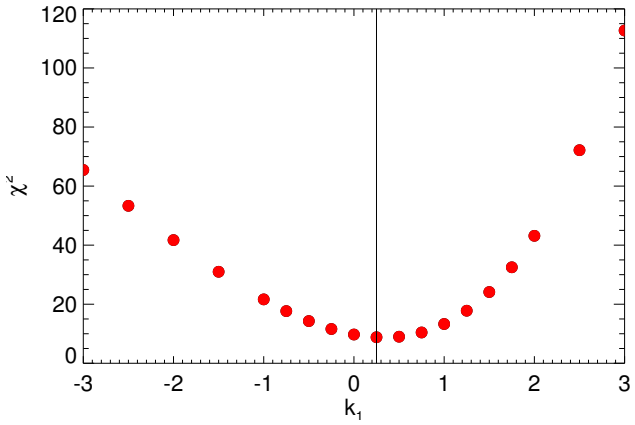

Figure 13. Chi-square parameter as a function of k_1 for discharge 35372. A minimum is obtained for $k_1 \sim 0.2$.

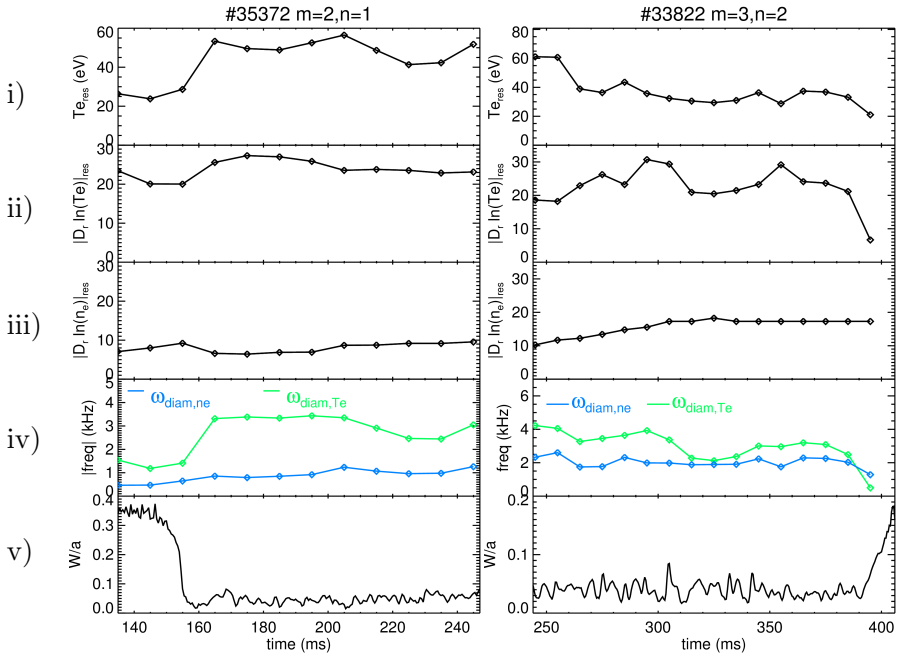

Figure 14. Temporal evolution of several quantities related to the diamagnetic frequency for the $m = 2, n = 1$ TM in shot 35372 (left panels) and the $m = 3, n = 2$ TM in shot 33822 (right panels). From top to bottom: electron temperature (i), absolute value of the T_e logarithmic radial derivative (ii), absolute value of the n_e logarithmic radial derivative (iii). All these quantities are estimated at the resonant radius. The *absolute values* of ω_{diam,T_e} and ω_{diam,n_e} are shown in panel (iv). Panel (v) displays the estimated island width normalized to the minor radius.

As a final comment on this point, it is worth to add that we also attempted to interpret our experimental data by using a model in which the electron diamagnetic term plays no role and hence the plasma flow only would determine mode rotation. From a physical point of view, this would correspond to having TM islands frozen within the ion flow and not within the electron one. A sensitivity analysis, not shown, predicts an optimal value $k_1 \approx -4$. This value, even considered our limited interpretative capabilities, appears, on the basis of the theoretical expectation, somehow unrealistic, as this would require very high α, hence Z_{eff} values (see again Figure 1 in [25]).

3.5. Analysis of ω_{diam}

The contributions of density and temperature within the diamagnetic frequency are now investigated in more detail for the $m = 2$, $n = 1$ and $m = 3$, $n = 2$ modes, described in figures 9a and 10a respectively. Let's consider the splitting

$$\omega_{diam} = \omega_{diam,T_e} + \omega_{diam,n_e} \tag{26}$$

$$\omega_{diam,T_e} = CT_e \frac{d(\ln T_e)}{dr}\bigg|_{r_s}; \quad \omega_{diam,n_e} = CT_e \frac{d(\ln n_e)}{dr}\bigg|_{r_s}; \quad C = \frac{5}{3}\frac{m}{er_sB_\phi} \tag{27}$$

We assumed $T_i = 2/3T_e$. The factor C, related to the magnetic equilibrium, does not

significantly change within the examined time intervals ($q_{cyl}(a)$ is almost constant there: see figures 7, 10b). Hence, C can be regarded as a shot-dependent coefficient. Note that

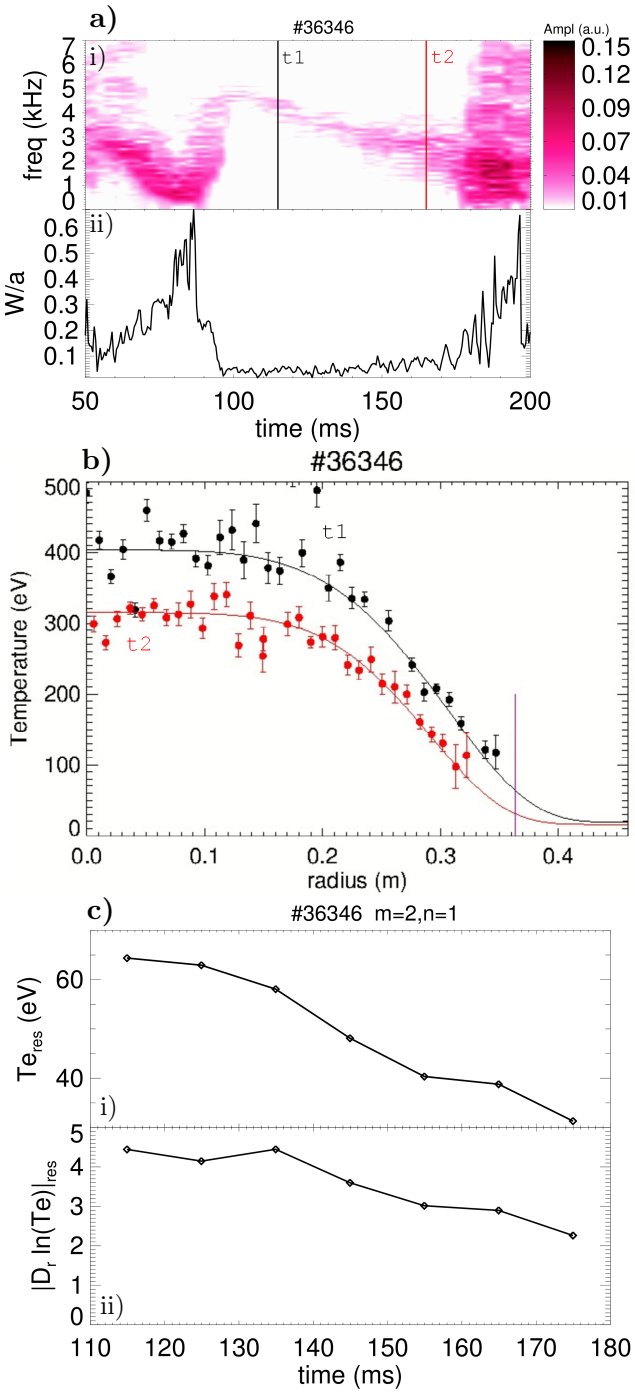

Figure 15. Analysis of the m=2, n=1 TM in shot 36346. a): spectrogram (i) and time trace of W/a (ii). b): T_e profile, acquired and fitted, at two different time instants t_1 and t_2 (highlighted in (a) by vertical lines), corresponding to significantly different TM frequencies. The violet vertical line denotes the resonant $q = 2$ radius. c): time traces of T_e (i) and $|d(\ln T_e)/dr|$ (ii) estimated at the resonant radius, during the slowing down phase.

ω_{diam,T_e} depends on T_e only, whereas ω_{diam,n_e} combines both T_e and n_e.
In figure 14 the temporal behavior of ω_{diam,T_e} and ω_{diam,n_e} are displayed, in absolute value, for the two cases considered in figures 9a and 10a. The time evolution of T_e, $|d(\ln T_e)/dr|$, $|d(\ln n_e)/dr|$, all taken at r_s, and of the estimated normalized island width are also plotted. As shown in panels (iv), the ω_{diam,T_e} is more important than ω_{diam,n_e}, both in absolute terms and as far as the variations are concerned. In fact, $|d(\ln T_e)/dr|$ (panels *ii*) is larger and more variable than $|d(\ln n_e)/dr|$ (panels *iii*).
The W/a drop at time $t \approx 150ms$ in shot 35372 (panel v on the left) correlates with an increase of both T_e and $|d(\ln T_e)/dr|$ at the resonant surface, which determines an increase of the absolute value of ω_{diam,T_e}: this explains the mode spin-up reported in figure 9a at this time. The same process, in the opposite sense, takes place in the final part of shot 33822: the island growth correlates with the local decrease of temperature and its logarithmic derivative, which determines a drop of ω_{diam,T_e}, and therefore of the mode frequency, as reported in figure 10a. Note that, the density profile, hence ω_{diam,n_e}, is less sensitive to the island width variations (panels *iii*).
In these two examples the variations of T_e at the resonant surface are concordant with those of $d(\ln T_e)/dr$, and enhance the overall effect onto ω_{diam,T_e}. This synergistic behavior is found also in the further example considered in figure 15. Being characterized by a long slowing down phase of the $m = 2, n = 1$ TM, this case is well suited to correlate the modifications of the frequency with those of the temperature profile. Indeed, the slowing down of the magnetic frequency associates with a similar slow decrease of the temperature parameters (value and logarithmic derivative) at the resonant surface. A weak, but steady W increase can be also detected during this phase. The full temperature profile is also provided at two time instants: note that the modifications of $T_e(r)$ have a *global* character.

3.6. Discussion

The above analysis suggests a correlation between the TM island fast rotation and the kinetic profiles. The results can be summarized as follows.
i) In the RFX-mod tokamak, TM rotates with the electron fluid at the resonant surface, because their frequency can expressed by the sum of ω_{flow}, the frequency of a mode frozen in the ion fluid, and ω_{diam}, representing the diamagnetic drift. Moreover, the latter contribution is dominant. However, the diamagnetic effect should be less important in larger devices, due to its inverse dependence on the minor radius and on the toroidal magnetic field.
ii) This drift mainly depends on the temperature derivative at the resonant surface: the dominant contribution ω_{diam,T_e} can be written as $CdT_e/dr|_{r_s}$.
iii) This local derivative is affected by the TM island through global modifications of the temperature profile. In particular, the following sequence is proposed: an *increase/decrease* of the island width involves an *increase/decrease* of the energy transport, hence a *decrease/increase* of T_e, which *slows-down/spins-up* the diamagnetic drift

along with the TM frequency.
It should be notice that this is not the customary interpretation, as far as the TM slowing down process is concerned. In fact, this is generally due to the interaction with the mirror currents induced onto the vacuum-vessel, developing an electromagnetic torque on the *ion fluid* at the resonant surface. If such an effect was relevant in the considered cases, the correlation between the diamagnetic frequency and the mode frequency would not be so strict. Rather, a significant modification of ω_{flow}, not observed, would occur. In the section 4, further evidences are presented, supporting the inadequacy of the purely electromagnetic slowing-down model in the RFX-mod discharges.

4. Slowing down analysis

The RFX-mod analysis above presented links the dynamics of TM fast rotation to that of the kinetic profiles, temperature in particular. In this case, the electromagnetic interaction with the vacuum-vessel mirror currents should be a secondary effect. In this section, a more quantitative assessment of this statement is provided, showing that the electromagnetic torque model does not fit the pre-disruptive slowing down phase. Let's consider the $m = 2$, $n = 1$ TMs of several RFX-mod shots, taken in a subset of the database displayed in figures 5 and 6, which benefits from clearer data than those referring to the $m = 3$, $n = 2$ mode. The related magnetic frequencies are plotted as a function of time in figure 16a. Most of the initial values, before the slowing down, stand

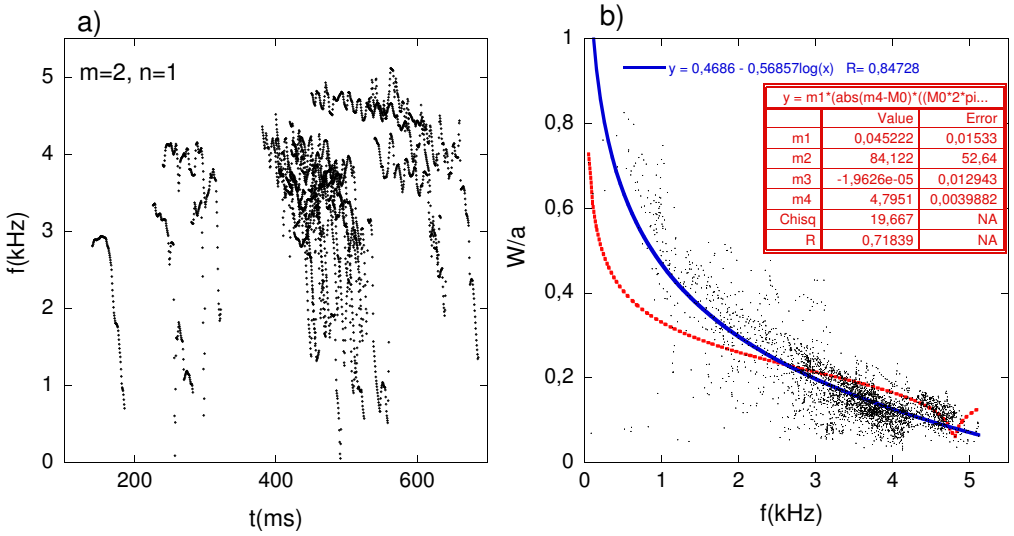

Figure 16. Slowing down analysis for the $m = 2$, $n = 1$ TM for several RFX-mod tokamak shots. a) magnetic frequencies vs time (only the frequency slowdown phase for each analyzed discharge is shown in the graph); b) island width vs frequency: the blue line is the logarithmic fit ($y = a_1 + a_2\, log(x)$), whereas the red dashed line is the fit (29).

between $4 \div 5$ kHz. Therefore, we take these frequencies unaltered, without applying

any normalization. In figure 16b the normalized island width is plotted against these frequencies. A continuous slowing down occurs as the mode amplitude increases, roughly fitted by a logarithmic function (blue continuous line). The further fit (red dotted line) wants to assess the compatibility of the data with the electromagnetic braking model. Now such a fit is described. Modelling the vacuum vessel only by the innermost thin shell (i.e. $\tau_v = 0$: choice justified by the analysis presented in paragraph 2.2), and taking the outermost copper shell as ideal, the braking model predicts the following relationship between the mode frequency f and the island width [3]:

$$C\left(\frac{W}{a}\right)^4 \frac{2\pi f\tau_w}{(2\pi f\tau_w)^2 + E_{vess}^2} = f_0 - f; \qquad E_{vess} = E_{ww} - \frac{E_{vw}E_{wv}}{E_{vv}} \tag{28}$$

The constant C incorporates the viscosity and the poloidal flow damping time, as well as other equilibrium related parameters, whereas f_0 is the mode frequency for $W/a \ll 1$. By inverting (28), in order to express W/a as a function of the frequency, the following interpolating function of the data displayed in figure 16b is tried:

$$\frac{W}{a} = m_1 \left\{ |m_4 - f| \left[(2\pi f\tau_w)^2 + m_2^2 \right] / (2\pi f\tau_w) \right\}^{1/4} + |m_3| \tag{29}$$

In this expression f is in kHz and τ_w in ms. The coefficients of the fit are denoted m_i, with $i = 1, ..., 4$. In particular, m_4 gives an estimate of f_0 and m_2 of E_{vess}. In order to make the fit viable, two changes have been made with respect to equation (28): the difference $f_0 - f$ is taken in absolute value, and an offset m_3, expected to be small, is added. There is little dependence of the result on τ_w: here it is fixed at 1.5ms. The quality of the fit (29) is rather poor, as can be seen in the figure. Moreover, while m_4 turns out to be in the correct range, and m_3 is small as expected, $m_2 \sim 84$ is quite larger than the estimate $|E_{vess}| \sim 18$ given by Newcomb's equation.

The model represented by (28) is based on the thin-shell approximation, already discussed in section 2.2. We tried to compare the slowing down data also with the electromagnetic braking model based on a thick-shell approximation, though this hypothesis does not seem justified for the RFX-mod vessel. According to equation (73) of reference [3], equation (28) is replaced by

$$C\left(\frac{W}{a}\right)^4 = f^{\frac{1}{2}}(f_0 - f) \tag{30}$$

with all the numerical constant encapsulated within C. Using an interpolating function based on such a model, indeed we obtained a even worse fit with respect to that based on the thin-shell model, presented in figure 16b.

The conclusion is that the electromagnetic model cannot describe the slowing down of the $m = 2$, $n = 1$ tearing mode in the presented RFX-mod discharge. This statement is applied to the fast rotation only and it does not imply that TMs do not interact with the passive or active conductive structures. In fact, the electromagnetic torque determines the final wall-locking, so far as this phenomenon takes place at the end of the slowing down, being the unique mechanism able to stop the TM island rotation in the laboratory frame, above an amplitude threshold [3]. Moreover, the electromagnetic

model well describes the slow rotation regime, mentioned at the end of paragraph 2.5, which is induced by the feedback action as mitigation of the wall-locking condition [6].

5. Conclusions

Tearing modes represent a concern for the control of fusion plasmas, being characterized by magnetic islands that degrade confinement and increase the plasma wall interaction. In tokamak, the growth of their amplitude and the concomitant slowing down of their spontaneous fast rotation, can lead to a disruption. In this paper we try to understand the mechanisms which determine the TM island rotation, by analyzing the high frequency regime observed in the circular tokamak plasmas of RFX-mod. This work complements previous analyses focused on the slow rotation frequency regime induced by the magnetic feedback [6]. The analysis is mostly based on the data from a set of large-bandwidth in-vessel edge probes located in front of the plasma, and therefore not affected by screening from the passive conductive structures. This is an improvement with respect to [6], where the out-vessel sensors of RFX-mod were instead used. The procedure by which the amplitude and frequency of the modes are extracted from the raw measurements is quite standard, but not straightforward. Then, these harmonics have been compared with two models dealing with different features of the tearing mode physics: the good agreement found provides a validation both for the processing of the magnetic data and the models themselves.

The first model, based on Newcomb's equation and the thin-shell dispersion relation, describes the radial profile of the perturbation, as well as the frequency-dependent boundary conditions imposed by the screening effect of the vacuum-vessel. It is used to extrapolate the magnetic perturbation harmonics inside the plasma, thus giving an estimate of the island width, according to the text-book formula, besides a more refined estimate of the external radial excursion of the island. This analysis has been applied to the database, already considered in [6], of discharges disrupted after slowing down of the dominant TM ($m = 2$,$n = 1$ or $m = 3$,$n = 2$). The new results confirm that disruptions can occur even without a locking to the wall. Furthermore, the external radius of the island gets close or even beyond the plasma surface in the pre-disruptive phase for both $m = 2$,$n = 1$ and $m = 3$,$n = 2$ modes. This suggests that, though TM could be not the original cause of the disruption, it surely takes a part in the final process.

The second model deals with the mode rotation, which is obtained from a frozen condition of the island within the electron fluid. Then, the frequency can be expressed by the sum of a frequency ω_{flow} related to the ion velocity (i.e. the frequency of an island frozen within the ion-fluid) and a frequency ω_{diam} related to the diamagnetic effects. Due to the relatively few cases where both temperature and density can be measured with a sufficient accuracy to estimate the diamagnetic frequency, the comparison between the frequencies from the model and those from the in-vessel magnetic analysis cannot be done on a statistical basis. Nonetheless, the indications from the examined cases are quite clear. i) The magnetic frequencies are well reproduced by the model,

hence TM island co-rotates with the electron fluid. ii) The diamagnetic frequency dominates over the ion-flow related frequency. iii) A correlation between the variations of the frequency, the island width and the temperature profile is found, suggesting a transport-based interpretation of the mode slowing-down/spin-up: a growing island slows down by increasing the energy transport, hence decreasing the temperature profile and consequently the diamagnetic drift; a quenching island should instead spins up through the opposite process.
It must be said that this does not represent the standard interpretation of the TM island rotation dynamics, which is generally ascribed to the electromagnetic torque developed by the interaction between the island and the mirror currents induced onto the passive conductive structures. We have also shown that this electromagnetic model does not fit the magnetic frequencies, in the pre-disruptive slowing phase, thus confirming the previous interpretation based on the kinetic profiles. However, this concerns only the fast rotation and it does not imply that TMs are not subject to the interaction with the conductive structures. In fact, the wall-locking, if it takes place at the end of the slowing down phase, can be produced only by the electromagnetic torque. Finally, we note that the inverse dependence of ω_{diam} on the minor radius and the toroidal field might reduce the relevance of this effect in large devices.

6. Appendix A: Mode detection from in-vessel edge signals

This appendix is devoted to present the techniques used for mode identification from in-vessel edge signals. In particular, in the following, the procedure sequence for the identification of a given mode with poloidal and toroidal numbers m, n is described:
1) A spatial Fourier transform is performed at each time sample on the poloidal array signals, providing the perturbation components with $m \leq 3$ (regardless to n).
2) A discrete Fourier transform (DFT) in the frequency domain is applied to the time series of each spatial harmonic component in order to associate the proper frequency to the various coherent modes.
It is worth noting that the use of the DFT has been chosen to determine the frequency of each mode as an alternative and more reliable technique with respect to the use of the time derivative of the phase of each single spatial harmonic. This choice, which is based on a time sliced division of the signals, considered as independent realization of the same process, gives a more statistically meaningful result even if less time-resolved. This has been forced by a relatively low signal-to-noise ratio collected by the used in-vessel coils. It must, indeed, be reminded that such probes, measuring the time derivative of the edge magnetic fields, had been originally designed to detect magnetic fluctuations in the RFP configuration, which can be significantly larger than in the Tokamak. Obviously, the use of the Fourier decomposition is justified in time windows in which mode frequency and amplitude remain almost constant.
The Fourier spectrogram (i.e. the frequency power spectrum resolved on time windows)

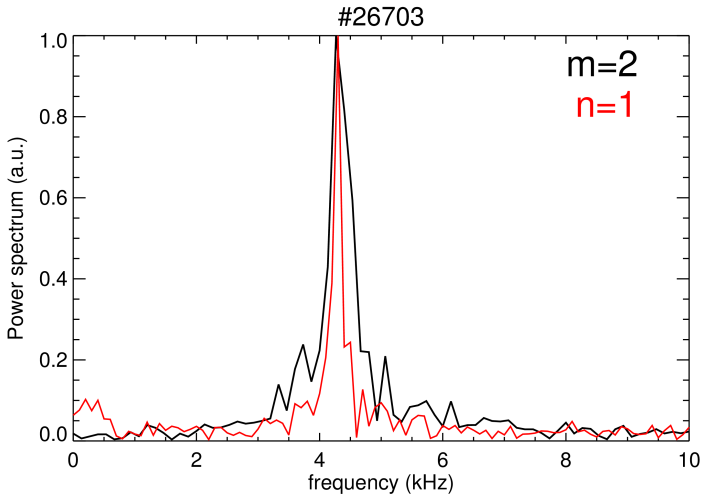

Figure 17. Frequency spectrum of the $m = 2$ (black curve) and $n = 1$ (red curve) magnetic fluctuation performed at time $t = 320ms$ for the #26703 tokamak discharge. Amplitudes are normalized to unity. Both $m = 2$ and $n = 1$ components exhibit a dominant frequency at about 4.3 kHz.

is thus performed on each m-component and the dominant associated frequency determined.

The frequency power spectrum for the $m = 2$ harmonic component, in a given time interval during the flat-top phase of a typical tokamak discharge, is shown in figure 17. A dominant peak is clearly seen, centered around 4.3 kHz.

3) The spatial Fourier transform is performed on the toroidal array signals, which allow the discrimination of the various n-harmonics up to $n \leq 24$ (regardless to m).

4) The associated dominant frequencies are determined by means of Fourier spectrogram analysis.

5) The m,n modes are then identified by matching the dominant frequencies obtained at points 2) and 4).

In figure 17, the frequency power spectrum obtained for shot #26703 for the $n = 1$ component is superimposed, as a red curve, to the $m = 2$ one (for the same time interval). As clearly seen, the two spectra exhibit a dominant peak, with a coincident central frequency, allowing the recognition of a $m = 2, n = 1$ mode, that we identify as a resistive tearing mode, internally resonant at the position where the cylindrical edge safety factor q_{cyl} is equal to 2. Also the $m = 3, n = 2$ TMs and the $m = 3, n = 1$ toroidal side-bands of the $m = 2, n = 1$ TMs, discussed through this paper, have been detected with the same technique.

It is important to note that, during the slowing down phase, a different approach to the one previously described has been adopted in order to improve the time resolution in the determination of the mode frequency. Indeed, thanks to the increase of the mode amplitude, the phase of the dominant m harmonic $\Phi(t)^m$ is determined in a more reliable way, so that the mode frequency can be obtained at any given time instant as $f(t)^m = \dot{\Phi}(t)^m/2\pi$.

7. Appendix B: derivation of Equation (10)

Equation (10) stems from the following approximation, which can be applied fairly well either to a high-frequency $m = 2$, $n = 1$ or $m = 3$, $n = 2$ mode, screened by the vacuum vessel, in the region $r \geq r_s$:

$$|\psi^{m,n}| = |\psi_s| \left(1 - \frac{x}{x_w}\right) \ , \qquad x = (r - r_s)/r_s \geq 0 \ , \qquad x_w = (r_w - r_s)/r_s \quad \text{(B-1)}$$

Let's consider the cylindrical, helical formalism described in [27]: every quantity depends on r and the helical angle $u = m\theta - n\phi$. Denoting by χ the helical flux, which is a real quantity, standard relations are:

$$r b_r = \frac{\partial \chi}{\partial u} \quad \text{(B-2)}$$

$$r\, \mathbf{B} \cdot \nabla u = m B_\theta - n \frac{r}{R} B_\phi = -\frac{\partial \chi}{\partial r} \quad \text{(B-3)}$$

We also assume the expansion $\chi(r, u) = \chi_0(r) + \chi_1(r) cos(u)$. In this case equations (1) and (B-2) are conciliated by taking $\chi_1 = |\psi^{m,n}|$ and including in $\psi^{m,n}$ a factor 2, which encapsulates the complex conjugate harmonic's (i.e. $-m$,$-n$) contribution. Hence, $\chi_1(r_s) = |\psi_s|$. As far as the zeroth-order component is concerned, (B-3) becomes

$$-\frac{\partial \chi_0}{\partial r} = m B_{\theta 0} - n \frac{r}{R} B_{\phi 0} = F_0(r) \quad \text{(B-4)}$$

For the $m = 2$, $n = 1$ mode of a tokamak equilibrium F_0 can be well approximated by a linear decreasing function, hence χ_0 by a parabolic function, in the region beyond the resonant surface:

$$F_0(r) \cong F'_{0s}\, r_s\, x \ \ \rightarrow \ \ \chi_0 \cong -\frac{1}{2} F'_{0s}\, r_s^2\, x^2 \ , \quad x \geq 0 \ , \quad F'_{0s} \equiv F'_0(r_s) < 0 \quad \text{(B-5)}$$

A magnetic surface identified by $\chi(r, u) = \chi_0(r) + \chi_1(r) cos(u) = \overline{\chi}$ is described by a parametric equation for $x(u)$, obtained from (B-1), (B-5):

$$x^2 - \left(\frac{\xi}{x_w} cosu\right) x + \xi cosu + C = 0 \ , \ \ \xi = \frac{2\chi_1(r_s)}{r_s^2 |F'_{0s}|} = \frac{W^2}{8 r_s^2} \ , \ \ C = -\frac{2\overline{\chi}}{r_s^2 |F'_{0s}|} \quad \text{(B-6)}$$

Use has been made of definition (9). Note that ξ is a small positive parameter. The approximations leading to (B-6), valid for $x \geq 0$, still holds for $x < 0$, but not too far from the resonant surface. The discriminant of (B-6) is $\Delta(u, C)/4 = -\xi cosu \left[1 - \frac{\xi}{4x_w^2} cosu\right] - C = \Delta(u, 0)/4 - C$. Given the smallness of ξ, we can take the term in parenthesis to be positive. Hence, $\Delta(u, 0)$ is monotonically increasing from $u = 0$ to $u = \pi$, and then monotonically decreasing up to $u = 2\pi$. Therefore, for $C < \Delta(0, 0)/4 = -\xi \left[1 - \frac{\xi}{4x_w^2}\right]$ two real solutions of x are given at any u: this is the region outside the magnetic island. Instead, for $\Delta(0, 0)/4 < C < \Delta(\pi, 0)/4 = \xi \left[1 + \frac{\xi}{4x_w^2}\right]$ two real solutions of x are given only within the intervals $u_C < u < 2\pi - u_C$, being $\Delta(u_C, C) = 0$: this is the region of the magnetic island. The island separatrix is

identified by $C = \Delta(0,0)/4 = -\xi\left[1 - \frac{\xi}{4x_w^2}\right]$: here, the maximum x, attained at $u = \pi$, is

$$max[x]_{separatrix} = \frac{1}{2}\left(\frac{W}{r_s} - \frac{\xi}{x_w}\right) \tag{B-7}$$

Using the x and ξ definitions within (B-7), formula (10) is finally obtained.

[1] P. H. Rutherford. Nonlinear growth of the tearing mode. The Physics of Fluids, 16(11):1903–1908, 1973.

[2] R. Fitzpatrick. Interaction of tearing modes with external structures in cylindrical geometry (plasma). Nuclear Fusion, 33(7):1049, 1993.

[3] R. Fitzpatrick, S. C. Guo, D. J. Den Hartog, and C. C. Hegna. Effect of a resistive vacuum vessel on dynamo mode rotation in reversed field pinches. Physics of Plasmas, 6(10):3878–3889, 1999.

[4] M. F. M. De Bock, I. G. J. Classen, C. Busch, R. J. E. Jaspers, H. R. Koslowski, B. Unterberg, TEXTOR Team, et al. The interaction between plasma rotation, stochastic fields and tearing mode excitation by external perturbation fields. Nuclear Fusion, 48(1):015007, 2008.

[5] P. Innocente, P. Zanca, M. Zuin, T. Bolzonella, and B. Zaniol. Tearing modes transition from slow to fast rotation branch in the presence of magnetic feedback. Nuclear Fusion, 54(12):122001, 2014.

[6] P. Zanca, R. Paccagnella, C. Finotti, A. Fassina, G. Manduchi, R. Cavazzana, P. Franz, C. Piron, and L. Piron. An active feedback recovery technique from disruption events induced by m=2, n=1 tearing modes in ohmically heated tokamak plasmas. Nuclear Fusion, 55(4):043020, 2015.

[7] T. Bolzonella, N. Pomaro, G. Serianni, and D. Marcuzzi. New wide bandwidth in-vessel magnetic measurement system for RFX. Review of scientific instruments, 74(3):1554–1557, 2003.

[8] G. Serianni, T. Bolzonella, R. Cavazzana, G. Marchiori, N. Pomaro, L. Lotto, M. Monari, and C. Taliercio. Development, tests, and data acquisition of the integrated system of internal sensors for RFX. Review of scientific instruments, 75(10):4338–4340, 2004.

[9] R. Fitzpatrick. Formation and locking of the "slinky mode" in reversed-field pinches. Physics of Plasmas, 6(4):1168–1193, 1999.

[10] F. Gnesotto, P. Sonato, W. R. Baker, A. Doria, F. Elio, M. Fauri, P. Fiorentin, G. Marchiori, and G. Zollino. The plasma system of RFX. Fusion engineering and design, 25(4):335–372, 1995.

[11] C. G. Gimblett. On free boundary instabilities induced by a resistive wall. Nuclear fusion, 26(5):617, 1986.

[12] P. Zanca, L. Marrelli, R. Paccagnella, A. Soppelsa, M. Baruzzo, T. Bolzonella, G. Marchiori, P. Martin, and P. Piovesan. Feedback control model of the m= 2, n= 1 resistive wall mode in a circular plasma. Plasma Physics and Controlled Fusion, 54(9):094004, 2012.

[13] J. A. Wesson. Tokamaks 3rd edn. Oxford: Clarendon, 2004.

[14] B.J. Sun, D. Lopez-Bruna, M.A. Ochando, and M.A Pedrosa. Low frequency coherent modes in TJ-II plasmas. In 41st European Physical Society Conf. on Plasma Physics, ECA (Berlin, Germany), volume 38, page P2.090, 2014.

[15] F. L. Waelbroeck. Natural velocity of magnetic islands. Physical review letters, 95(3):035002, 2005.

[16] Bruce D. Scott, A. B. Hassam, and J. F. Drake. Nonlinear evolution of drift-tearing modes. Phys. Fluids, 28(1):275, 1985.

[17] Q. Yu, S. Günter, Y. Kikuchi, and K. H. Finken. Numerical modelling of error field penetration. Nuclear Fusion, 48(2):024007, 2008.

[18] P. Zanca and D. Terranova. Reconstruction of the magnetic perturbation in a toroidal reversed field pinch. Plasma physics and controlled fusion, 46(7):1115, 2004.

[19] P. Innocente, S. Martini, A. Canton, and L. Tasinato. Upgrade of the RFX CO2 interferometer

using in-vessel optics for extended edge resolution. Review of scientific instruments, 68(1):694–697, 1997.

[20] F. Auriemma, R. Lorenzini, M. Agostini, L. Carraro, G. De Masi, A. Fassina, M. Gobbin, E. Martines, P. Innocente, P. Scarin, et al. Characterization of particle confinement properties in RFX-mod at a high plasma current. Nuclear Fusion, 55(4):043010, 2015.

[21] A. Fassina, M. Gobbin, S. Spagnolo, P. Franz, and D. Terranova. Characterization of small thermal structures in RFX-mod electron temperature profiles. Plasma Physics and Controlled Fusion, 58(5):055017, 2016.

[22] M. Zuin, W. Schneider, A. Barzon, R. Cavazzana, P. Franz, E. Martines, M.E. Puiatti, P. Scarin, and E. Zampiva. Ion temperature measurements by means of a neutral particle analyzer in RFX-mod plasmas. In 38th EPS Conference on Plasma Physics 2011, EPS 2011 - Europhysics Conference Abstracts, volume 35 2, pages 1844–1847, 2011.

[23] L. Carraro, M. E. Puiatti, F. Sattin, P. Scarin, and M. Valisa. Toroidal and poloidal plasma rotation in the reversed field pinch RFX. Plasma physics and controlled fusion, 40(6):1021, 1998.

[24] P. Zanca. Avoidance of tearing modes wall-locking in a reversed field pinch with active feedback coils. Plasma Physics and Controlled Fusion, 51(1):015006, 2009.

[25] Y. B. Kim, P. H. Diamond, and R. J. Groebner. Neoclassical poloidal and toroidal rotation in tokamaks. Physics of Fluids B: Plasma Physics, 3(8):2050–2060, 1991.

[26] L. Piron, D. Bonfiglio, P. Piovesan, B. Zaniol, F. Auriemma, L. Carraro, L. Chacón, L. Marrelli, M. Valisa, M. Veranda, et al. 3d magnetic fields and plasma rotation in rfx-mod tokamak plasmas. Nuclear Fusion, 53(11):113022, 2013.

[27] D. Bonfiglio, D. F. Escande, P. Zanca, and S. Cappello. Necessary criterion for magnetic field reversal in the reversed-field pinch. Nuclear Fusion, 51(6):063016, 2011.